sample (without containing CNFs) were (i) 1627.63 and 1419.35 cm^{-1} (carboxylate), (ii) 947.84 cm^{-1} (α 1 → 4 linkage), and (iii) 890.95 cm^{-1} (α-L-gulopyranuronic ring), respectively. While for Na^+–ALG/CNFs, they were (i) 1613.16 and 1413.57 cm^{-1}, (ii) 943.98 cm^{-1}, and (iii) 887.8 cm^{-1}, respectively. These shifts (decrease) in the alginate characteristic bands again indicate alginate being attached tightly to the CNFs. The characteristic band of the sugar backbones increased from 811.88 cm^{-1} in the reference sample (alginate alone) to 814.77 cm^{-1} in the Na^+–ALG/CNFs, suggesting the attaching of alginate to the CNFs is governed by their sugar backbones.

From these experimental observations, we suggest that complexes, i.e., alginate/CNFs, were formed in the aqueous Na^+–ALG/CNFs colloidal solutions. This can be attributed to the hydrophobic interactions occurring between the sugar backbones of alginate and the external surfaces of CNFs. The negatively charged moieties of the alginate/CNFs complex, i.e., the carboxylate groups, produce high zeta potentials, which stabilize the complexes in the aqueous electrolyte solutions.

Biocompatibility of Alginate/CNFs. Adsorbents of high biocompatibility are highly desirable in environmental remediation, especially in the case of in situ elimination of the targeted pollutants from the contaminated animals. In the in vitro experimental study with normal human fibroblasts (HF) as the typical cells, the relative cell growth (RCG), which was calculated by dividing a mean value of the treated cells by a mean value of untreated cells (cultured with 5% FBS), was found as high as 100 ± 5% at 1-day and 2-days after the administration of Na^+–ALG/CNFs and/or Na^+–ALG. RCG were better than 85 ± 5% even at 7-days after the administration. On the other hand, in the in vivo experimental study with rats as the typical animals, an increase in white blood cells (WBC) was observed at 1-week and 2-weeks after the administrations (WBC, μL^{-1}, increased from 5100 in the untreated rat to 7700 and 8100 in the rats given the control, while they increased to 7900 and 8400 for the rats given the Na^+–ALG/CNFs colloids). The β-globulin fraction also increased from 16.2% in the untreated rat to 21.7% and 21.5% in the rats treated with Na^+–ALG and/or Na^+–ALG/CNFs. Deep plica of the glandular stomach were observed at 1-week after the administration with Na^+–ALG and/or Na^+–ALG/CNFs. Changes in the other parameters were smaller than ±10%. All hematological and biochemical data recovered to normal levels 3-weeks after the administration. Both in vitro- and in vivo-experiments showed that alginate and the alginate/CNFs complexes had no or very little detrimental impact on the cells/animals studied in this study.

Adsorptive Capability of the Vesicles. Three gelling solutions, (i) an aqueous solution containing sodium alginate alone at 20.0 mg/mL, (ii) CNFs at 0.5 mg/mL highly-dispersed in 20.0 mg/mL Na^+–ALG solution, and (iii) CNFs at 0.5 mg/mL simply dispersed (mixed by ultra-sonication for 5 min) in 20.0 mg/mL Na^+–ALG solution, were prepared and used for preparing the reference vesicles (those did not contain CNFs), the vesicles containing highly dispersed CNFs, and the vesicles containing low-dispersed CNFs, respectively. A typical microscopic observation of the vesicles containing highly dispersed CNFs are shown in Fig. 6. Vesicles having a diameter in the range of 400–800 micrometers were observed. The nozzle diameter strongly influenced the vesicle size. Generally, vesicles are produced with an average diameter two times larger than the nozzle diameter. However, the average vesicle diameter can be adjusted by about ±20% by varying the jet velocity and the vibration frequency. Kilogram quantities of the vesicles can be produced within a few hours using this encapsulation system. The Ba^{2+}–ALG/CNFs composite vesicles are both chemically and mechanically stable, and are much heavier than water (hence it is easy to isolate the vesicles from water).

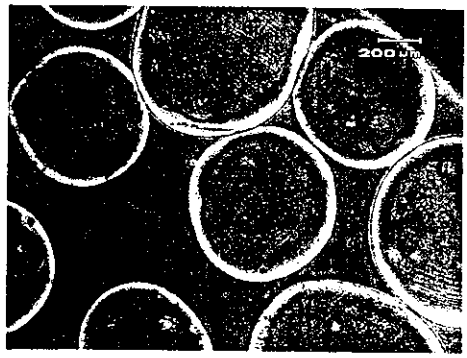

Fig. 6. Microscopic observation of the Ba^{2+}–alginate coated vesicles containing highly dispersed CNFs. The vesicles were produced using an aqueous colloidal solution containing 0.50 mg/mL CNFs and 20.0 mg/mL Na^+–ALG as the gelling solution with an aqueous solution containing 100 mM $BaCl_2$ as the gelatinizing solution.

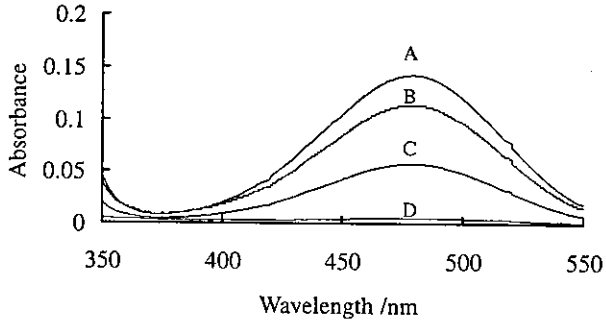

Fig. 7. UV–vis absorptions of an aqueous solution containing 30.0 μM ethidium bromide (A-trace); 15 mL of this 30 μM ethidium bromide solution being mixed with, the Ba^{2+}–alginate vesicles (reference vesicles; B-trace), the vesicles containing low-dispersed CNFs (C-trace), and the vesicles containing highly dispersed CNFs (D-trace) at 10 min after the solution/vesicles mixing.

Ethidium ions were chosen as the typical DNA-interactive species. They are highly water-soluble and used worldwide as an intercalating fluorescent dye for detecting DNA. Fifteen millilitres of the model contaminated water (prepared by dissolving ethidium bromide in deionized water at a concentration of 30.0 μM) was mixed with 10.0 mL of the vesicles. At about ten minutes after the mixing, approximately 3 mL of the bulk-phase solutions were collected and were measured using a UV–vis spectrometer. Figure 7 shows the results. The absorbance of the model contaminated water before the treatment, i.e., the 30.0 μM ethidium bromide aqueous solution, at

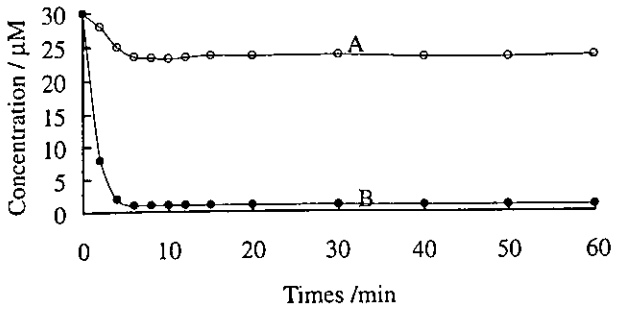

Fig. 8. Changes in concentrations of ethidium ions as a function of the contact time for a 15.0 mL of an aqueous solution containing 30.0 μM ethidium bromide after mixing that solution with 10.0 mL of the reference (Ba^{2+}–ALG) vesicles (upper-trace) and with the Ba^{2+}–ALG/CNFs composite vesicles (lower-trace).

480 nm was as high as 0.142. This, however, dropped to 4.9×10^{-3} after mixing this solution with the vesicles containing highly dispersed CNFs. Mixing the contaminated water with the vesicles containing low-dispersed CNFs also resulted in lowering the absorbance (which dropped to 0.058). This change, however, was much smaller than that observed for the vesicles containing highly dispersed CNFs. The control vesicles showed very little capability in trapping ethidium ions, suggesting the uptake of the targeted species is governed by the CNFs.

Figure 8 shows changes in the concentration of ethidium ions in the aqueous solution as a function of the contact time (15.0 mL of the 30.0 μM ethidium bromide aqueous solution were mixed with 10.0 mL of the vesicles containing the highly dispersed CNFs). The concentration of ethidium ions in the aqueous solution decreased rapidly as the contact time increased. It reached 0.98 μM and remained unchanged at about 8 min after mixing the solution with the Ba^{2+}–ALG/CNFs composite vesicles. In other words, 10.0 mL of the Ba^{2+}–ALG/CNFs composite vesicles took 0.44 μmol of the ethidium ions up and this uptake was accomplished within 8 min. The adsorptive experiments were performed three times, and the average value of the capacity for trapping ethidium ions for 10.0 mL of the vesicles obtained using the aqueous Na^{+}–ALG/CNFs colloidal solution containing 0.5 mg/mL for CNFs and 20.0 mg/mL for Na^{+}–ALG as the gelling solution was as high as 0.43 μmol (RDS $< \pm 1.2\%$).

Identical experiments were also performed using Ba^{2+}–alginate coated vesicles containing highly dispersed multi-walled carbon nanotubes (MWCNTs) as the adsorbents. MWCNTs (diameter, 20–40 nm; length, 1–5 μm, purity > 90%, as recommended by the manufacturer) were purchased from Nano Lab. and were used as received. Methods for preparing the aqueous Na^{+}–ALG/MWCNTs colloids, Ba^{2+}–ALG/MWCNTs composite vesicles, and for studying the capability for trapping ethidium ions were the same as for the CNFs. The capacity for trapping ethidium ions was found to be 0.42 μmol (RDS $< \pm 1.3\%$, $n = 3$) for 10.0 mL of the Ba^{2+}–ALG/MWCNTs vesicles obtained using an aqueous solution containing 0.50 mg/mL MWCNTs and 20.0 mg/mL Na^{+}–ALG as the gelling solution. This capacity value is virtually identical to that of the Ba^{2+}–ALG/CNFs composite vesicles, indicating the ethidium ions were unable to distribute in to the wall-nanopores of the CNFs. In other words, to accumulate the DNA-interactive chemicals in the wall-nanopores, it is necessary to expand the inter-planar distance among the graphite platelets of the CNFs.

Conclusion

Dispersing carbon nanofibers and/or nanotubes with a high uniformity into aqueous solutions is crucial for achieving the goal of utilizing these fascinating materials as high-performance adsorbents for absorbing/eliminating DNA-interactive type chemicals. The major goal in this study was achieved using alginate as the dispersing agent. Alginate is a non-toxic, naturally occurring linear polysaccharide (found widely in brown seaweed). Its gelling properties, together with its high biocompatibility, can generate a number of analytical-chemical, environmental, and biotechnological applications. Our dispersing approach based on alginate provides advantages over the previous methods:[19–25] (i) aqueous colloidal solutions containing CNFs and/or CNTs in pristine forms can be prepared in large-scales in a single step with a very simple manipulation procedure, (ii) the resultant aqueous colloids are highly biocompatible, and (iii) the colloids can be rearranged further as vesicles, providing a desirable approach to utilizing these nano-sized materials for macro-scaled applications. The selectivity of the Ba^{2+}–ALG/CNFs (also the Ba^{2+}–ALG/CNTs) composite vesicles for adsorbing DNA-interactive chemicals, especially for aromatic compounds having planar structures, is high. This is because the hexagonal arrays of the carbon atoms of the graphite sheets are the functional sites for trapping the targets. Note that columns packed with the entire CNFs and/or MWCNTs may also provide high trapping capabilities. They are, however, impractical for large-scale water treatment. This is because of the high backpressure that must be overcome to drive water through the packed column.

This study was partly supported by Grant-in-Aid for Research on Nano-medicine #H14-nano-021 from the Ministry of Health, Labor and Welfare.

References

1 E. C. Miller and J. A. Miller, *Cancer*, **47**, 2327 (1981).
2 B. N. Ames, *Science*, **204**, 587 (1979).
3 W. P. Watson, C. Bleasdale, and B. T. Golding, *Chem. Br.*, **1994**, 661.
4 K. Iwata, T. Sawadaishi, S. Ninishimura, S. Tokura, and N. Nishi, *Int. J. Biol. Macromol.*, **18**, 149 (1996).
5 M. Yamada, K. Kato, K. Shindo, M. Nomizu, M. Haruki, N. Sakairi, K. Ohkawa, H. Yamamoto, and N. Nishi, *Biomaterials*, **22**, 3121 (2001).
6 M. Yamada, K. Kato, M. Nomizu, N. Sakairi, K. Ohkawa, H. Yamamoto, and N. Nishi, *Chem.—Eur. J.*, **8**, 1407 (2002).
7 M. Yamada, K. Kato, M. Nomizu, K. Ohkawa, H. Yamada, H. Yamamoto, and N. Nishi, *Environ. Sci. Technol.*, **36**, 949 (2002).
8 D. Umeno, T. Kano, and M. Maeda, *Anal. Chim. Acta*, **365**, 101 (1998).
9 S. Iijima, *Nature (London)*, **354**, 56 (1991).

10 S. Iijima and T. Ichihashi, *Nature (London)*, **363**, 603 (1993).
11 Y. Cai, G. Jiang, J. Liu, and Q. Zhou, *Anal. Chem.*, **75**, 2517 (2003).
12 R. Q. Long and R. T. Yang, *J. Am. Chem. Soc.*, **123**, 2058 (2001).
13 A. Chambers, C. Park, R. K. Baker, and N. M. Rodriguez, *J. Phys. Chem. B*, **102**, 4253 (1998).
14 N. M. Rodriguez, *J. Mater. Res.*, **8**, 3233 (1996).
15 L. Jiang, L. Gao, and J. Sun, *J. Colloid Interface Sci.*, **260**, 89 (2003).
16 H. E. Ries, *Nature (London)*, **226**, 72 (1970).
17 N. P. Chandia, B. Matushiro, and A. E. Vasquez, *Carbohydr. Polym.*, **46**, 81 (2001).
18 H. Ronghua, D. Yumin, and Y. Jianhong, *Carbohydr. Polym.*, **52**, 19 (2003).
19 W. Zhao, C. Song, and P. E. Pehrsson, *J. Am. Chem. Soc.*, **123**, 5348 (2002).
20 V. Georgakilas, N. Tagmatarchis, D. Pantarotto, A. Bianco, J.-P. Briand, and M. Prato, *Chem. Commun.*, **2002**, 3050.
21 M. J. O'Connell, P. Boul, L. M. Ericson, C. Huffman, Y. Wang, E. Haroz, C. Kuper, J. Tour, K. D. Ausman, and R. E. Smalley, *Chem. Phys. Lett.*, **342**, 265 (2001).
22 G. I. Dovbeshko, O. P. Repnytska, E. D. Obraztsova, and Y. V. Shtogun, *Chem. Phys. Lett.*, **372**, 432 (2003).
23 A. Star, D. W. Steuerman, J. R. Heath, and J. F. Stoddart, *Angew. Chem., Int. Ed.*, **14**, 41 (2002).
24 R. Bandypoadhyaya, E. Native-Roth, O. Regev, and R. Yerushalmi-Rozen, *Nano Lett.*, **2**, 25 (2002).
25 N. Nakashima, S. Okuzono, H. Murakami, T. Nakai, and K. Yoshikawa, *Chem. Lett.*, **32**, 456 (2003).

Environ. Sci. Technol. 2004, 38, 6890−6896

Caged Multiwalled Carbon Nanotubes as the Adsorbents for Affinity-Based Elimination of Ionic Dyes

BUNSHI FUGETSU,*,† SHUYA SATOH,† TOSHIKAZU SHIBA,‡,§,∥ TAEKO MIZUTANI,‡ YONG-BO LIN,† NORIFUMI TERUI,† YOSHINOBU NODASAKA,⊥ KATSUSHI SASA,▽ KIYOKO SHIMIZU,○ TSUKASA AKASAKA,⊥ MASANOBU SHINDOH,⊥ KEN-ICHIRO SHIBATA,⊥ ATSURO YOKOYAMA,⊥ MASANOBU MORI,◆ KAZUHIKO TANAKA,◆ YOSHINORI SATO,△ KAZUYUKI TOHJI,△ SHUNITZ TANAKA,† NORIO NISHI,† AND FUMIO WATARI⊥

Graduate School of Environmental Earth Science, Hokkaido University, Sapporo 060-0810, Japan, Frontier Research Division, FUJIREBIO Inc., 51 Komiya, Hachioji, Tokyo 192-0031, Japan, Regenetiss Company, Ltd., 1-5-17 Okaya, Akabane, Nagano 394-0002, Japan, Department of Oral and Maxillofacial Surgery, Matsumoto Dental University School of Dentistry, Matsumoto, Japan, Graduate School of Dental Medicine, Hokkaido University, Sapporo 060-8586, Japan, Otsuka Electronic Company, Ltd., 1-6 Azuma-cho, Hachioji, Tokyo, Japan, Bioscience Division, Hokudo Company, Ltd., Abuta-cho, Abuta-gun, Hokkaido 049-5613, Japan, National Institute of Advanced Industrial Science and Technology at Seto, 110 Nishiibara-cho, Seto 489-0884, Japan, and Graduate School of Environmental Studies, Tohoku University, Sendai 980-8579, Japan

Multiwalled carbon nanotubes (MWCNTs) were used as the active elements for the first time for affinity-based elimination of ionic dyes. MWCNTs were encapsulated in cross-linked alginate (ALG) microvesicles using Ba^{2+} as the bridging ion. The Ba^{2+}−alginate matrix constitutes a cage which holds the physically trapped MWCNTs. The cage carries negative charges on its surface. The cage restricts the access of anions of large molecular weight, such as humic acids, because of electrostatic repulsion. The cage also restricts the access of colloids of large size, because of size exclusion. Ionic dyes partition into the cage and then are captured by MWCNTs probably on the basis of van der Waals interactions occurring between the hexagonally arrayed carbon atoms in the graphite sheet of MWCNTs and the aromatic backbones of the dyes. As a result of these interactions the target species, namely, the ionic dyes, are eliminated efficiently by the MWCNTs of Ba^{2+}−ALG/MWCNT composite adsorbents. The adsorptive capacities for elimination of acridine orange, ethidium bromide, eosin bluish, and orange G (the model species used for this study) were found as high as 0.44, 0.43, 0.33, and 0.31 μmol, respectively, for 1.0 mg of the caged MWCNTs. Adsorptive experiments with carbon nanofibers and activated carbons as the adsorbents were also performed. The MWCNT-based adsorbents provided the best capability for the affinity-based elimination of these targeted species. Biocompatibility experiments performed in vitro and in vivo provided promising results, suggesting potential applications of the caged MWCNTs in in situ environmental remediation.

Introduction

Dyes have long been recognized to be capable of causing environmental contaminations. First, dyes, especially the azo-type dyes (*1*), are suspected to be carcinogenic and are known to have potent acute and/or chronic effects on exposed organisms, depending on the exposure time and dye concentration. Second, dyes are capable of absorbing/reflecting sunlight; this can have a strong detrimental effect on the growth of bacteria to levels sufficient to biologically degrade impurities (*2*, *3*). Moreover, dyes are highly visible to the human eye; this can cause aesthetic contamination even at very low concentrations. Wastewaters from colorant industrials (such as from the textile, pulp, paper, and carpet manufacturing industries) contain dyes which should be eliminated to avoid environmental contaminations. A number of promising techniques have been established for elimination of dyes from contaminated waters. Physical adsorption appears to offer the best advantages (*4*−*7*), although the chemical degradation (*8*−*10*) and the biodegradation approaches (*11*−*13*) also find applications.

Here, we report experimental data on the first use of carbon nanotubes as the active elements for affinity-based elimination of dyes. Carbon nanotubes (CNTs) are the tubular derivatives of fullerenes first discovered by Iijima in 1991 (*14*). CNTs can be classified into multiwalled carbon nanotubes (MWCNTs) (*14*) and single-walled carbon nanotubes (SWCNTs) (*15*), according to the graphene layers in the wall of the nanotubes. Because of their unusual morphology and unique electronic, mechanical, and chemical properties, CNTs have been the subject of many theoretical and experimental studies since their discovery. With the great progress in synthesizing/purifying CNTs, attention has been recently directed to their fields of practical applications. So far, potential application of CNTs to environmental protection/remediation has been very little explored. An environmental analytical chemical study of Cai and co-workers demonstrated that cartridges filled with MWCNTs are capable of extracting bisphenol A, 4-*n*-nonylphenol, 4-*tert*-octylphenol (*16*), and several phthalate esters (*17*) from contaminated waters. Cartridges or columns packed with CNTs may provide high elimination capabilities; they are, however, impractical for large-scale water treatment. This is because of the high back-pressure that must be overcome to drive water through the packed cartridges and/or columns. Another adverse factor currently restricting the application of CNTs to environmental

* Corresponding author phone and fax: +81-11-706 2272; e-mail: hu@ees.hokudai.ac.jp.
† Graduate School of Environmental Earth Science, Hokkaido University.
‡ FUJIREBIO Inc.
§ Regenetiss Co., Ltd.
∥ Matsumoto Dental University School of Dentistry.
⊥ Graduate School of Dental Medicine, Hokkaido University.
▽ Otsuka Electronic Co., Ltd.
○ Hokudo Co., Ltd.
◆ National Institute of Advanced Industrial Science and Technology at Seto.
△ Tohoku University.

10.1021/es049554i CCC: $27.50
Published on Web 10/27/2004

protection/remediation is their high costs, which are about 1000 times higher than those of the traditional activated carbons.

These difficulties encountered in environmental applications with CNTs as the active elements were overcome by formation of "caged CNTs". As defined in this laboratory, the caged CNTs are cross-linked alginate vesicles containing physically trapped CNTs. The cross-linked alginate constitutes a polymer "cage", holding physically trapped, highly dispersed CNTs. The polymer cage allows bidirectional diffusion of chemicals of small molecular weight but restricts the freedom of kinetic distribution of molecules and/or colloids of large size. Ionic dyes partition into the vesicles and then are captured by CNTs on the basis of affinity-based adsorption. Humic acids and colloidal particles, on the other hand, are unable to diffuse across the cage. This provides a desirable approach to protect the active elements from being damaged by adsorbing chemicals and/or colloids of large size. The caging (encapsulating) technique is also a practical approach to overcome the high cost and/or high-pressure difficulties encountered in the use of CNTs for environmental remediation.

Materials and Methods

Dispersion of MWCNTs Using Alginate. Sodium alginate (the viscosity and pH at 28 °C were 376 cP and 7.10, respectively, for a 10.0 mg/mL aqueous solution) was obtained from Wako Chemical Industries (Osaka, Japan). Sodium alginate (Na^+−ALG) was dissolved in deionized water to prepare the aqueous Na^+−ALG solution at a concentration of 10.0 mg/mL. MWCNTs (CVD products, outer diameter 15 ± 5 nm, length 1−5 μm, purity >90%, as stated by the manufacturer) were purchased from Nanolab (Massachusetts) and were used as received. MWCNTs were introduced to an aqueous Na^+−ALG (10.0 mg/mL) solution and were then well-mixed by a combination of high-shear mixing and sufficient ultrasonication. The uniformity of the aqueous Na^+−ALG/MWCNT colloids was measured by calculating the linearity of the calibration curve for MWCNTs in the Na^+−ALG/MWCNT colloidal solutions using UV−vis at 254 nm as the detection method. ζ potentials of the aqueous Na^+−ALG/MWCNT colloids were measured using an electrophoretic light scattering spectrophotometer (ELS-8000, Otsuka Electronics, Osaka, Japan). FT-IR spectra of Na^+−ALG in the aqueous Na^+−ALG/MWCNT colloids were measured using an FT/IR-460 (Jasco, Tokyo, Japan).

Preparation of Cross-Linked Alginate Microvesicles. An IER-20 encapsulation system (Inotech, Dottikon, Switzerland) was used for vesicle preparation. The aqueous Na^+−ALG/MWCNTs colloids (precursor solution) were forced into the pulsation chamber using a syringe pump. These aqueous colloids were then passed through a precisely drilled sapphire nozzle (nozzle size 200 μm) and were separated into droplets of equal size on exiting the nozzle. These droplets passed through the electrostatic field between the nozzle and an O-ring electrode and acquired electrostatic charges on their surfaces. Electrostatic repulsion forces dispersed the droplets as they fell into the hardening (coagulation) solution, which was an aqueous solution containing 100 mM barium chloride (see the schematic diagram in Figure 1). The resultant vesicles were rinsed thoroughly with deionized water using a 100 μm mesh sieve. Reference vesicles (without containing MWCNTs), vesicles containing activated carbons, and vesicles containing CNFs were also prepared under identical encapsulation conditions. The activated carbons (activated charcoal, powder) were obtained from Wako Chemical Industries, while CNFs (diameter 50−250 nm, length 2−15 μm, purity >90%) were synthesized in the laboratory on the basis of the chemical vapor deposition method (*18*). The Ba^{2+}−ALG vesicles are both mechanically and chemically stable, and

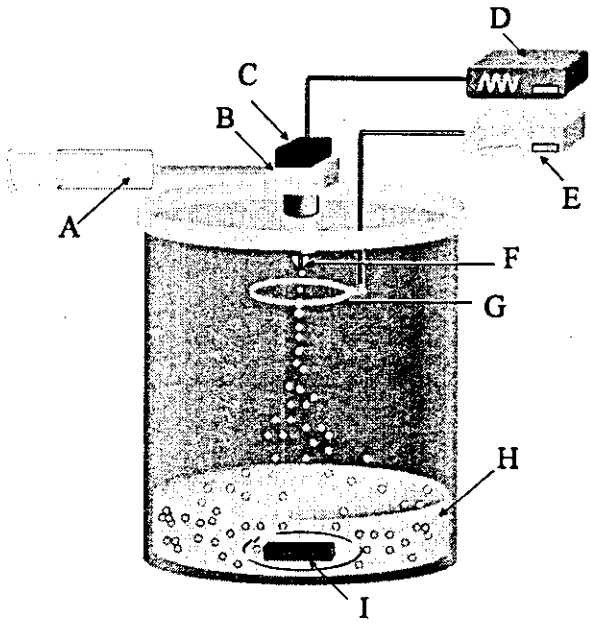

FIGURE 1. Schematic diagram of the encapsulation system: (A) syringe pump; (B) pulsation chamber; (C) vibration system; (D) frequency generator; (E) electrostatic charge generator; (F) nozzle; (G) O-ring electrode; (H) coagulation solution; (I) magnetic stirrer.

are much heavier than water; hence, it is easy to isolate the vesicles from the treated water.

Biocompatibility Studies. Balb c/3T3 cells were used to perform the in vitro experiments. The cells were seeded to 48-multiwell plates at 6000 cells/well (300 μL/well) and cultured in Dulbecco's modified Eagle's minimal essential medium (DMEM) containing 10% fetal bovine serum (FBS) for 3 days at 37 °C. The media containing the alginate vesicles were prepared by suspending 100, 50, and 10 mg of vesicles in 1.0 mL of DMEM containing 10% FBS to give solutions containing 100, 50, and 10 mg/mL alginate vesicles, respectively. The medium of the 48-multiwell plates was replaced with 300 μL of the media containing the alginate vesicles, and the cells were further incubated at 37 °C. After 48 h of incubation, the cell proliferation was evaluated by 3-(4,5-dimethylthiazol-2-yl)-5-(3-carboxymethoxyphenyl)-2-(4-sulfophenyl)-2*H*-tetrazolium (MTS) assay. For MTS assay, the media were replaced with 100 μL of Eagle's minimal essential medium (without Phenol Red), and 25 μL of a mixture of MTS (Promega) and phenazine methosulfate solution (2.0 mg/mL MTS, 0.92 mg/mL phenazine methosulfate) was added to each well. After incubation for 1 h at 37 °C, the absorbance at 490 nm of each well was measured. The cell number was quantified by means of the bioreduction activity of viable cells.

Twelve 10-week-old Crj:CD(SD) IGS male rats (purchased from Charles River Japan, Inc.) were used to perform the in vivo experiments. These rats were quarantined and acclimatized for 6 days. Three were used without any administration, while the others were dosed orally using a stomach tube for 1 week. The dose volumes were 5.0 mL/kg of body mass. Gross observations and body masses were recorded daily. During the term of observation, the animals were starved for 16 h and anesthetized, and then blood and serum samples were collected. Necropsy was also performed for observing changes in the glandular stomach.

Adsorption Studies. A given volume of the model-contaminated water containing a known quantity of dye was mixed with a known volume of the vesicles using a 100 mL conical-bottomed test tube. The concentration of dye in the aqueous phase was measured using a UV spectrophotometer (Jasco UV-550). Acridine orange and ethidium bromide

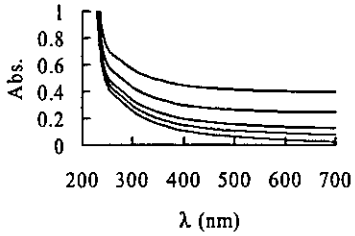

FIGURE 2. UV–vis absorption spectrum of the dispersing solution (which was prepared by dissolving sodium alginate in deionized water at a concentration of 10.0 mg/mL, the bottom trace) and that of the dispersed MWCNTs at concentrations of 100, 50, 25, and 10 ppm (from top to bottom, respectively).

(cationic type) and eosin bluish and orange G (anionic type) were used as the model species to represent the water-soluble, ionic dyes. The adsorptive experiments were performed using Ba^{2+}–ALG composite vesicles (i.e., the control vesicles), Ba^{2+}–ALG vesicles containing MWCNTs (caged MWCNTs), vesicles containing CNFs (caged CNFs), and vesicles containing activated carbons (caged ACTC) as the adsorbents. Humic acids (HAs; obtained from Wako Chemical Industries) were used as the model species to represent water-soluble, naturally occurring compounds of high molecular weights.

Encapsulation of CNTs in Ba^{2+}–ALG vesicles is a desirable approach to restrain adsorbents of small size; this, however, may create mass-transfer problems. To figure out this point, the adsorptive experiments were also performed using the as-purchased MWCNTs (also CNFs and activated carbons) as the adsorbents. A high-pressured filtration process (the aqueous solution containing dye mixed with MWCNTs, CNFs, or activated carbons was filtered through two stacked polycarbonate filters of 100 nm pore size) was necessary to remove the adsorbents.

Results and Discussion

Aqueous Alginate/MWCNT Colloids. Normally, CNTs (including both SWCNTs and MWCNTs) are seen as powders of visible size because of the strong van der Waals attractions occurring among the individuals. To encapsulate CNTs in vesicles, it was necessary to disperse CNTs with high uniformity in the encapsulating solutions. Approaches to dispersion of CNTs in organic solutions have been developed, mainly based on chemical attachment of appropriate blocks to the carboxylic groups (which are produced by oxidation of CNTs using strong acids) (*19*, *20*). The so-called side-wall organic functionalization technique (*21*, *22*) also finds application. On the other hand, wrapping of water-soluble polymers around CNTs is a simpler yet powerful technique for dispersing CNTs in aqueous solutions. Polymers used in previous studies for CNT dispersion are poly(vinylpyrrolidone) (PVP), poly(styrenesulfonate) (PSS) (*23*), deoxyribonucleic acid (DNA) (*24–26*), starch (*27*), and Arabic gum (*28*). In this study, we use alginate for dispersing the as-purchased powders of entangled CNTs in aqueous solutions. The uniformity of MWCNTs in the aqueous alginate solution was calculated by measuring the linearity of the calibration curve for MWCNTs in the aqueous Na^+–ALG/MWCNT colloidal solutions at 254 nm. The linearity, r^2, was found to be better than 0.9981, indicating MWCNTs were being dispersed in the aqueous Na^+–ALG colloidal solutions with high uniformity. Samples used for deriving the calibration curve were the aqueous Na^+–ALG solutions containing 0, 10, 25, 50, and 100 ppm MWCNTs, with the concentration of Na^+–ALG in each sample being fixed at 10.0 mg/mL. Figure 2 shows UV–vis absorption spectra of the samples; a characteristic absorption derived from the dispersed MWCNTs is seen around 254 nm. The stability of the aqueous Na^+–ALG/MWCNT colloids was measured by calculating the concentration of the MWCNTs versus the sediment time, similar to the method reported by Jiang and co-workers (*29*). Changes in the MWCNT concentrations were found to be smaller than 1.3% over 7 days at room temperature.

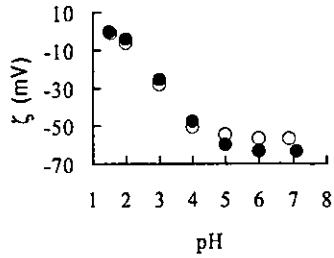

FIGURE 3. ζ potential of the Na^+–ALG/MWCNT colloids (●; MWCNTs, 100 ppm; Na^+–ALG, 10.0 mg/mL) and ζ potential of the dispersing solution (○; Na^+–ALG alone, 10.0 mg/mL) as a function of pH.

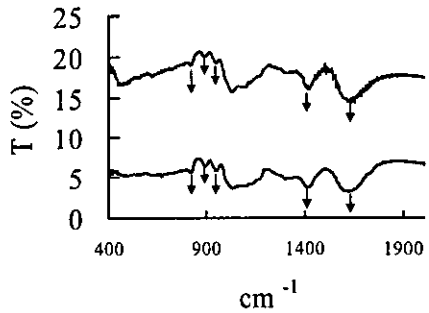

FIGURE 4. FT-IR spectra of Na^+–ALG (upper trace) and Na^+–ALG/MWCNT colloids (lower trace) in the solid state using the potassium bromide (KBr) pellet method.

The ζ potential was measured by calculating the colloid velocities on the basis of the Helmholtz–Smoluchowski equation ($\zeta = 4\pi\mu\eta/D$, where μ, η, and D are the electrophoretic mobility, viscosity, and dielectric constant of the liquid in the boundary layer, respectively) (*30*). The ζ value for the Na^+–ALG/MWCNT colloids was found to be as high as −63.50 mV. This again indicates the high stability of the Na^+–ALG/MWCNT colloids. Figure 3 shows the ζ versus pH plots for the Na^+–ALG/MWCNT colloids and that for the aqueous solution containing Na^+–ALG alone. At higher pH values (5.01, 6.02, 7.10), the alginate/MWCNT colloids showed slightly higher absolute ζ potentials than the sample containing sodium alginate alone, while, at the lower pH values, the ζ potentials for both samples were virtually identical. A decrease in the absolute value of ζ is seen for both samples as the pH decreases (the pH values of the samples were adjusted using 1.0 M HCl). MWCNTs precipitated as the pH reached 2.01 and 1.51. The high ζ potential value and thereby the high stability of the alginate/MWCNT colloids are a result of formation of alginate/MWCNT complexes in the colloidal solution. FT-IR spectral measurement (Figure 4) gives chemical evidence to support this conclusion. Frequencies of the carboxylic group of alginate for the alginate/MWCNT sample shifted from 1628.6 and 1417.4 cm^{-1} to 1618.9 and 1413.5 cm^{-1}, indicating alginate interacting with MWCNTs. On the other hand, the frequency of the α 1–4 linkage for the alginate/MWCNT sample decreased from 949.8 to 945.8 cm^{-1}, suggesting the interaction of alginate with MWCNTs is governed by the hydrophobic sugar backbones of alginate. The frequency of β-mannuronic residues (M) at 892.9 cm^{-1} and that of α-guluronic residues (G) at 815.7 cm^{-1} were observed, suggesting the alginate used for this study is built up in the M–G–M arrangement (*31*, *32*).

Biocompatibility of the Caged MWCNTs Adsorbents of high biocompatibility are highly desirable for in situ environmental remediation. In the in vitro experiments with Balb

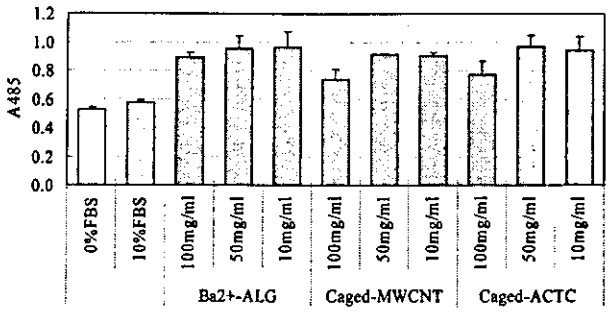

FIGURE 5. Effects of Ba^{2+}–ALG vesicles, caged MWCNTs, and caged ACTC on cell proliferation.

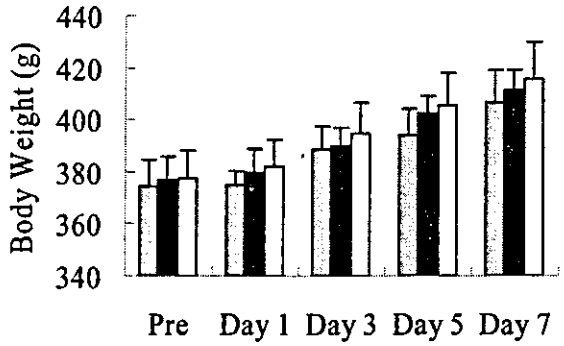

FIGURE 6. Body mass changes as a function of the number of dosed days. The rats were treated with the Ba^{2+}–alginate control vesicles (left-hand column), caged MWCNTs (central column), and caged ACTC (right-hand column).

c/3T3 cells as the typical cells, cells cultured with the caged MWCNTs showed higher cell density than cells cultured without the vesicles (Figure 5). Similar results were also observed for cells cultured with the control vesicles (Ba^{2+}–alginate vesicles) and vesicles containing activated carbons (caged ACTC). The vesicle provided some beneficial effects on cell attachment/growth, and as a result, higher cell densities were provided. The media containing caged MWCNTs and caged ACTC at 100 mg/mL gave lower cell densities than the media containing the control vesicles at the same concentration. The caged MWCNTs and the caged ACTC may adsorb the essential factors, such as the trace amount of growth factors, for cell growth. On the other hand, in the in vivo experimental study with rats as the typical animals, the caged MWCNTs and the caged ACTC showed some enhancement effects on body mass gain (Figure 6). Hematological data and biochemical data for the vesicle-dosed rats were found to be identical to those for the untreated rats (the verification values were $<\pm 8.9\%$, $n = 3$). A change of the deep plica of the glandular stomach was not observed for the vesicle-dosed rats. Both in vitro and in vivo experiments demonstrated that the caged MWCNTs (also the caged ACTC and the Ba^{2+}–alginate vesicles) are highly biocompatible with the cells/animals studied in this study.

Adsorption Studies. Four precursor solutions, (i) an aqueous solution containing sodium alginate alone at 10.0 mg/mL, (ii) MWCNTs, (iii) CNFs, and (iv) ACTC, each at 0.1 mg/mL, being highly dispersed in 10.0 mg/mL Na^+–ALG solution, were prepared and used for preparing the reference vesicles (Ba^{2+}–ALG), caged MWCNTs, caged CNFs, and caged ACTC, respectively. A typical microscopic observation of the vesicles containing MWCNTs, i.e., the caged MWCNTs, is shown in Figure 7. Vesicles having a diameter in the range of 400–600 μm were observed. The nozzle diameter strongly influenced the vesicle size. Generally, vesicles are produced with an average diameter 2 times larger than the nozzle diameter. However, the average vesicle diameter can be adjusted by about $\pm 20\%$ by varying the jet velocity and the vibration frequency. Kilogram quantities of the vesicles can be produced within a few hours using this encapsulation system.

A 15 mL sample of model-contaminated water (prepared by dissolving acridine orange (AO) in deionized water at a concentration of 10.0 μM) was mixed with 3.0 mL of the vesicles. About 30 min after the mixing, approximately 3 mL of the bulk-phase solution was collected and measured using a UV–vis spectrometer. Figure 8 shows the results. The absorbance of the model-contaminated water before the treatment, i.e., the 10.0 μM AO aqueous solution, at 492 nm, was as high as 0.38. This value, however, dropped to 0.037 and 0.042 after this solution was mixed with the vesicles containing MWCNTs and the vesicles containing CNFs, respectively. Vesicles containing activated carbons also showed the ability to lower the absorbance (which dropped to 0.071). This change, however, was smaller than that observed for the vesicles containing MWCNTs (also the vesicles containing highly dispersed CNFs). The control vesicles showed very little capability in trapping AO, suggesting the uptake of the targeted species is governed by the carbon particles. The capability in trapping ethidium bromide ((ET)Br) from the contaminated water was also found in the order caged MWCNTs > caged CNFs > caged ACTC $\gg$ control vesicles.

Figure 9 shows the experimental data on elimination of eosin bluish (EOB) obtained by mixing 15 mL of the model-contaminated water (prepared by dissolving EOB in deionized water at a concentration of 10.0 μM) with 3.0 mL of the vesicles. The caged MWCNTs showed the highest adsorptive capabilities, followed by the caged ACTC and then the caged CNFs, for elimination of EOB. The control vesicles (Ba^{2+}–ALG) showed no capability for adsorbing EOB. Similar results were also observed for elimination of orange G (OG).

The Ba^{2+}–ALG cage showed some detrimental (resistant) effects on mass transfer for elimination of anionic dyes (EOB and OG). This was observed by comparison of the rates of uptake of EOB using the caged MWCNTs and the as-purchased MWCNTs (MWCNT powder alone) as the active element. As can be seen in Figure 10A, the uptake of the targeted species was accomplished within 10 min when the MWCNT powders alone were used as the adsorbent. It, however, took 23 min to achieve the goal when the caged MWCNTs were used.

The resistant effects on mass transfer were extremely large for anions of large molecular weight. This was observed experimentally using HAs as the targeted species. As can be seen in Figure 10B, HAs showed high affinity toward MWCNTs in the powder forms but no affinity toward MWCNTs in the caged form. In other words, HAs were unable to diffuse across the Ba^{2+}–alginate cage. HAs exclusion can be attributed to the electrostatic repulsion and/or the size exclusion effect of the Ba^{2+}–ALG matrix. The selective permeation properties of the cage provide a desirable approach to protection of the active elements from being damaged by adsorbing chemicals of large molecular weights.

Table 1 summarizes the ultimate capacity for elimination of AO, (ET)Br, EOB, and OG for 1.0 mg of MWCNTs used in the caged and/or powder forms. Experimental data on the ultimate adsorptive capacity for the activated carbons and CNFs are also given in Table 1 for comparison. MWCNTs showed the highest capabilities for elimination of both the cationic and anionic types of the model species; this was irrespective of whether the powder form or the caged form was used as the adsorbent. CNFs gave higher capabilities than activated carbons for elimination of the cationic type of dyes (namely, AO and (ET)Br). On the other hand, however, activated carbons showed higher capabilities than CNFs for elimination of the anionic type of dyes (i.e., EOB and OG).

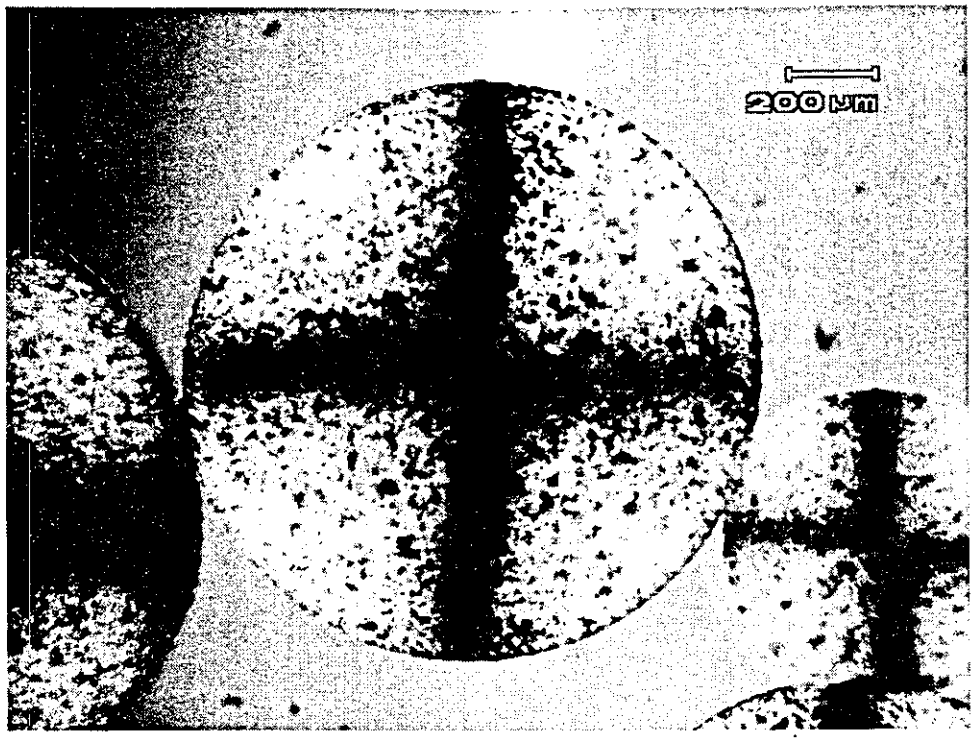

FIGURE 7. Microscopic observation of the Ba^{2+}–alginate-coated vesicles containing highly dispersed MWCNTs. The vesicles were produced using an aqueous colloidal solution containing 0.10 mg/mL (namely, 100 ppm) MWCNTs and 10.0 mg/mL Na^{+}–ALG as the precursor solution with an aqueous solution containing 100 mM $BaCl_2$ as the coagulation solution.

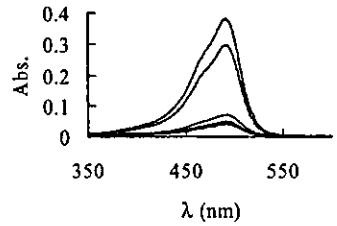

FIGURE 8. UV–vis absorption spectrum of an aqueous solution containing 10.0 μM AO and that of 15 mL of this 10.0 μM AO solution mixed with Ba^{2+}–alginate vesicles (reference vesicles), caged ACTC, caged CNFs, and caged MWCNTs (from top to bottom, respectively) 30 min after the solution/vesicle mixing.

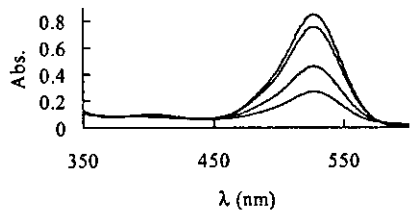

FIGURE 9. UV–vis absorption spectrum of an aqueous solution containing 10.0 μM EOB and that of 15 mL of this 10.0 μM EOB solution mixed with 3.0 mL of caged CNFs, caged ACTC, and caged MWCNTs (from top to bottom, respectively) 30 min after the solution/vesicle mixing. Note that the solution mixed with Ba^{2+}–alginate vesicles (reference vesicles) showed an absorption spectrum identical to that of the untreated solution.

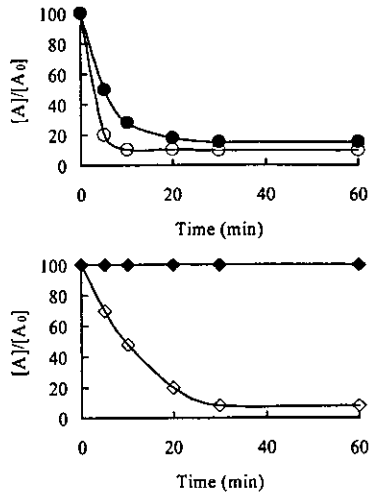

FIGURE 10. (A) Effects of the Ba^{2+}-cross-linked alginate cage on the rate of uptake of EOB by MWCNTs: (●) MWCNTs encapsulated in the cage; (○) MWCNTs alone. [A_0] = the initial concentration of EOB. [A] = the concentration of EOB in the aqueous solution found after the solution was mixed with the adsorbents. (B) Effects of the Ba^{2+}-cross-linked alginate cage on the rate of uptake of HAs by MWCNTs: (◆) MWCNTs encapsulated in the cage; (◇) MWCNTs alone. [A_0] = the initial concentration of HAs. [A] = the concentration of HAs in the aqueous solution found after the solution was mixed with the adsorbents.

MWCNTs offer the best capabilities for adsorbing dyes. This can be attributed to the fact that the hexagonally arrayed carbon atoms in the graphite sheets of MWCNTs are the active sites for trapping the targets. CNFs are built up also by hexagonally arrayed carbon atoms, but the 002 planes pile up along the direction of the fiber axis. These graphite platelets stack in a unique conformation in which only the edge sites are exposed (*33*). CNFs are typically highly defective and therefore should have a considerably large number of carboxylic groups on the exposed edges of the purified CNFs. The carboxylic groups are the beneficial sites for elimination of cationic dyes, and as a result, higher capabilities for elimination of AO and (ET)Br are obtained. These negatively charged groups, however, can have resistant effects on mass transfer for anionic dyes. The very low capability to eliminate EOB and OG by the CNF-based adsorbents gives the experimental evidence to support this conclusion.

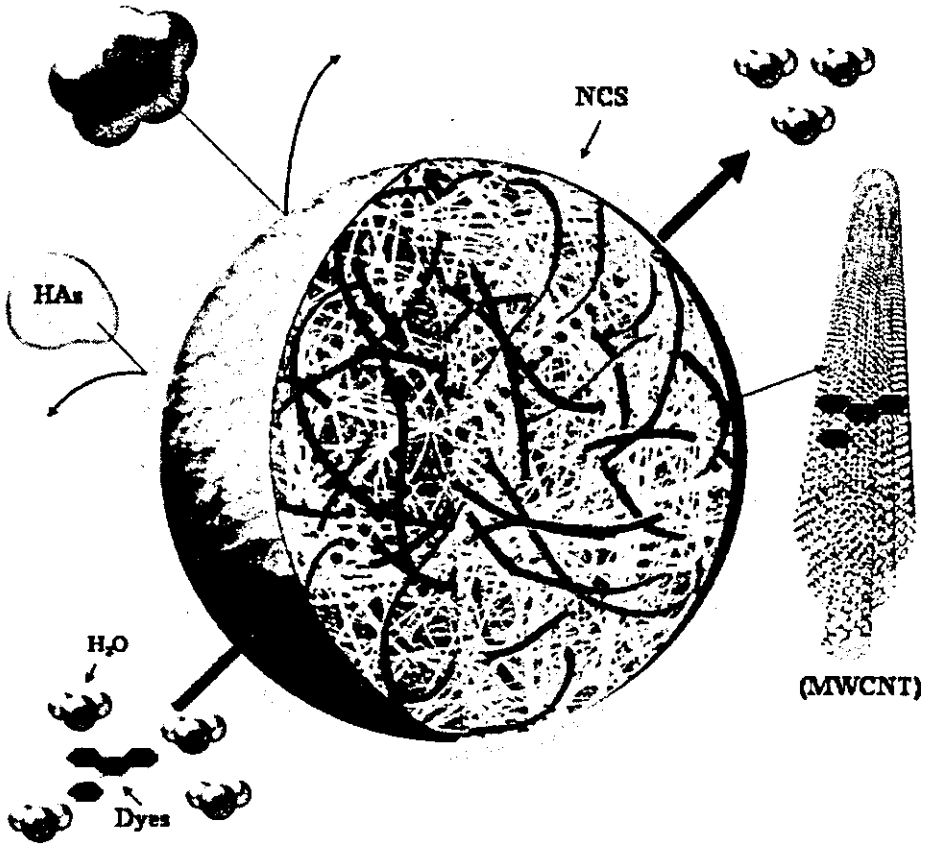

FIGURE 11. Schematic representation of the advantageous performances of the caged MWCNTs. The Ba^{2+}–alginate cross-linked matrix constitutes a cage which holds the physically trapped MWCNTs. The cage carries negative charges (NCS) on its surface. The cage restricts the access of anions of large molecular weights, such as HAs, because of electrostatic repulsion. The cage also restricts the access of CLS because of size exclusion. Dyes partition into the cage and are captured by MWCNTs probably on the basis of van der Waals interactions occurring between the hexagonally arrayed carbon atoms in the graphite sheet of MWCNTs and the aromatic backbones of the dyes. As a result of these interactions the target species, namely, the ionic dyes, are eliminated efficiently by the MWCNTs of the MWCNT/Ba^{2+}–ALG composite adsorbents.

TABLE 1. Adsorptive Capacity (μmol/mg) of MWCNTs, CNFs, and ACTC for Elimination of the Ionic Dye[a]

	MWCNT-P	C-MWCNT	CNF-P	C-CNF	ACTC-P	C-ACTC
AO	0.39	0.44	0.38	0.43	0.36	0.39
(ET)Br	0.37	0.43	0.36	0.42	0.35	0.37
EOB	0.37	0.33	0.09	0.06	0.25	0.19
OG	0.35	0.31	0.07	0.04	0.22	0.15

[a] Average values of three measurements (RSD < 1.8%). MWCNT-P = MWCNTs in the powder form (MWCNTs alone), and C-MWCNT = MWCNTs encapsulated in the cross-linked Ba^{2+}–alginate vesicle. CNF-P, ACTC-P, C-CNF, and C-ACTC have the same meanings as for MWCNTs. AO = acridine orange, (ET)Br = ethidium bromide, EOB = eosin bluish, and OG = orange G.

A model, as shown in Figure 11, is proposed to summarize the advantageous performances of the caged MWCNTs for elimination of the ionic dyes. The affinity elements, namely, MWCNTs, are encapsulated in Ba^{2+}–alginate vesicles of submillimeter size. This provides a desirable approach to restrain adsorbents of nanosize. The Ba^{2+}-cross-linked alginate matrix constitutes a cage. This cage restricts the access of anions of large molecular weight (also colloids of large size, CLS) while it allows the bidirectional distribution of chemicals of small molecular weights. HAs exclusion is probably due to the negatively charged surface (NCS) of the cage, although size exclusion may also be a possible explanation. Dyes were eliminated by MWCNTs probably on the basis of van der Waals attractions occurring between the aromatic backbones of dyes and the hexagonally arrayed carbon atoms in the graphite sheets of the MWCNTs. In addition, the caged MWCNTs could be reused by regenerating the vesicles with aqueous methanol or acetonitrile solutions. The caged MWCNTs may also be applicable for in situ elimination of dyes and/or other types of aromatic pollutants from the contaminated animal bodies. Experimental studies on the possibility of using the caged MWCNTs for in situ environmental remediation are under evaluation.

Acknowledgments

The very helpful comments provided by the reviews of this manuscript are gratefully acknowledged. This study was partly supported by a Grant-in-Aid for Research on Nanomedicine (No. H14-nano-021) from the Ministry of Health, Labor and Welfare of Japan.

Literature Cited

(1) Brown, M. A.; De Vito, S. C. Predicating azo dye toxicity. *Crit. Rev. Environ. Sci. Technol.* **1993**, *23*, 249–324.
(2) Slokar, Y. M.; Le Marechal, M. Methods of decolouration of textile wastewaters. *Dyes Pigm.* **1998**, *37*, 335–356.
(3) Strickland, A. F.; Perkins, W. S. Decolouration of continuous dyeing wastewater by ozonation. *Text. Chem. Color.* **1995**, *27*, 11–19.
(4) Pandit, P.; Basu, S. Removal of ionic dyes from water by solvent extraction using reversed micelles. *Environ. Sci. Technol.* **2004**, *38*, 2435–2442.
(5) Gupta, V. K.; Srivastava, S. K.; Mohan, D. Equilibrium uptake, sorption dynamics, process optimization, and column operations for the removal and recovery of malachite green from

wastewater using activated carbon and activated slag. *Ind. Eng. Chem. Res.* **1997**, *36*, 2207−2218.
(6) Garg V. K.; Amita M.; Kumar R.; Gupta R. Basic dye (methylene blue) removal from simulated wastewater by adsorption using Indian Rosewood sawdust: a timber industry waste. *Dyes Pigm.* **2004**, *63*, 243−250.
(7) Poots, V. J. P.; McKay, G.; Healy, J. J. The removal of acid dye from effluent using natural adsorbents-I peat. *Water Res.* **1976**, *10*, 1061−1066.
(8) Karkmaz, M.; Puzenat, E.; Guillard, C.; Herrmann, J. M. Photocatalytic degradation of the alimentary azo dye amaranth mineralization of the azo group to nitrogen. *Appl. Catal., B: Environ.* **2004**, *51*, 183−194.
(9) Zheng S.; Huang Q.; Zhou J.; Wang B. A study on dye photoremoval in TiO_2 suspension solution. *J. Photochem. Photobiol., A: Chem.* **1997**, *108*, 235−238.
(10) Ruppert G.; Bauer, R.; Heisler, G. UV-O_3, UV-H_2O_2, UV-TiO_2 and the photo-fenton reaction-comparison of advanced oxidation processes for wastewater treatment. *Chemosphere* **1994**, *28*, 1447−1454.
(11) More, A. T.; Vira, A.; Fogel, S. Biodegradation of *trans*-1,2-dichloroethylene by methane-utilizing bacteria in an aquifer simulator. *Environ. Sci. Technol.* **1989**, *23*, 403−406.
(12) Patil, S. S.; Shinde, V. M. Biodegradation studies of aniline and nitrobenzene in aniline plant waste water by gas chromatography. *Environ. Sci. Technol.* **1988**, *22*, 1160−1165.
(13) An H.; Qian Y.; Gu X.; Tang W. Z. Biological treatment of dye wastewaters using an anaerobic-oxic system. *Chemosphere* **1996**, *33*, 2533−2542.
(14) Iijima, S. Helical microtubules of graphitic carbon. *Nature (London)* **1991**, *354*, 56−58.
(15) Iijima, S.; Ichihashi, T. Single-shell carbon nanotubes of 1-nm diameter. *Nature (London)* **1993**, *363*, 603−605.
(16) Cai, Y.; Jiang, G.; Liu, J.; Zhou, Q. Multi-walled carbon nanotubes as a solid-phase extraction adsorbent for the determination of bisphenol A, 4-*n*-nonylphenol, and 4-*tert*-octyphenol. *Anal. Chem.* **2003**, *75*, 2517−2521.
(17) Cai, Y.; Jiang, G.; Liu, J.; Zhou, Q. Multi-walled carbon nanotubes packed cartridge for the solid-phase extraction of several phthalate esters from water samples and their determination by high-performance liquid chromatography. *Anal. Chim. Acta* **2003**, *494*, 149−156.
(18) Rodriguez, N. M. A review of catalytically grown carbon nanofibers. *J. Mater. Res.* **1993**, *8*, 3233−3250.
(19) Chen, J.; Hamon, M. A.; Hu, H.; Chen, Y.; Rao, A. M.; Eklund, P. C.; Haddon, A. Solution properties of single-walled carbon nanotubes. *Science* **1998**, *282*, 95−98.
(20) Zhao, W.; Song, C.; Pehrsson P. E. Water-soluble and optically pH-sensitive single-walled carbon nanotubes from surface modification. *J. Am. Chem. Soc.* **2002**, *124*, 12418−12419.
(21) Chen R. J.; Zhang Y.; Wang D.; Dai H. Noncovalent sidewall functionalization of single-walled carbon nanotubes for protein immobilization. *J. Am. Chem. Soc.* **2001**, *123*, 3838−3839.
(22) Georgakilas, V.; Tagmatarchis, N.; Pantarotto, D.; Bianco, A.; Briand, J.-P.; Prato, M. Amino acid functionalisation of water soluble carbon nanotubes. *Chem. Commun.* **2002**, 3050−3051.
(23) O'Connell, M. J.; Boul, P.; Ericson, L. M.; Huffman, C.; Wang, Y.; Haroz, E.; Kuper, C.; Tour, J.; Ausman, K. D.; Smalley, R. E. Reversible water-solubilization of single-walled carbon nanotubes by polymer wrapping. *Chem. Phy. Lett.* **2001**, *342*, 265−271.
(24) Dovbeshko, G. I.; Repnytska, O. P.; Obraztsova, E. D.; Shtogun, Y. V. DNA interaction with single-walled carbon nanotubes: a SEIRA study. *Chem. Phys. Lett.* **2003**, *372*, 432−437.
(25) Nakashima, N.; Okuzono, S.; Murakami, H.; Nakai, T.; Yoshikawa, K. DNA dissolves single-walled carbon nanotubes in water. *Chem. Lett.* **2003**, *32*, 456−457.
(26) Zheng, M.; Jagota, A.; Strano, M. S.; Santos, A. P.; Barone, P.; Chou, S. G.; Diner, B. A.; Dresselhaus, M. S.; Mclean, R. S.; Onoa, G. B.; Samsonidze, G. G.; Semke, E. D.; Usrey, M.; Walls, D. J. Structure-based carbon nanotubes sorting by sequence-dependent DNA assembly. *Science* **2003**, *302*, 1545−1548.
(27) Star, A.; Steuerman, D. W.; Heath, J. R.; Stoddart J. F. Starched carbon nanotubes. *Angew. Chem., Int. Ed.* **2002**, *14*, 2508−2512.
(28) Bandypoadhyaya, R.; Native-Roth, E.; Regev, O.; Yerushalmi-Rozen, R. Stabilization of individual carbon nanotubes in aqueous solutions. *Nano Lett.* **2002**, *2*, 25−28.
(29) Jiang, L.; Gao, L.; Sun, J. Production of aqueous colloidal dispersion of carbon nanotubes. *J. Colloid Interface Sci.* **2003**, *260*, 89−94.
(30) Ries, H. E. Microelectrophoresis measurements on polymeric flocculants alone and in excess with model colloids. *Nature (London)* **1970**, *226*, 72−73.
(31) Ronghua, H.; Yumin, D.; Jianhong, Y. Preparation and in vitro anticoagulant activities of alginate sulfate and its quaterized derivatives. *Carbohydr. Polym.* **2003**, *52*, 19−24.
(32) Chandia, N. P.; Matushiro, B.; Vasquez, A. E. Alginic acids in Lessonia Trabeculate: charaterization by formic acid hydrolysis and FT-IR spectroscopy. *Carbohydr. Polym.* **2001**, *46*, 81−87.
(33) Chambers, A.; Park, C.; Baker, R. K.; Rodriguez, N. M. Hydrogen storage in graphite nanofibers. *J. Phys. Chem. B* **1998**, *102*, 4253−4256.

Received for review March 22, 2004. Revised manuscript received September 14, 2004. Accepted September 14, 2004.

ES049554I

Recent developments in the *in situ* XAFS and related work for the characterization of catalysts in Japan

Kiyotaka Asakura*

Catalysis Research Center, Hokkaido University Kita 11-10,Ki-ta-ku, Sapporo 060-0811, Japan

This short review deals with some recent XAFS (X-ray absorption fine structure) applications to catalysts in Japan. The high transmission ability of X rays makes it possible to carry out *in situ* work on catalysts. First, *in situ* XAFS works under flow and high-pressure reaction conditions will be described. The time-resolved XAFS work will be another important topic because it can provide the possibility of observing the change of the reaction active site and the reaction intermediate. Finally, PTRF-XAFS will be described, which is a unique technique and provides three-dimensional local structures of highly dispersed surface species.

KEY WORDS: XAFS; PTRF-XAFS.

1. Introduction

XAFS (X-ray absorption fine structure) refers to a modulation appearing near the X-ray absorption edge and extending up to 1500 eV [1,2]. Since the first paper of Lytle Stern and Sayers in 1971 [3] on the Fourier analysis of XAFS, which provides the radial distribution curve around the X-ray absorbing atom, the XAFS spectra have been applied to many fields such as material sciences, environmental sciences and biological sciences [4]. XAFS has two remarkable features.

(1) The sample does not require crystallinity.
(2) Measurements can be done in the ambient atmosphere.

Catalyst materials are often used as a powder form to obtain a high surface area where active sites are randomly distributed. Therefore, the XAFS is a powerful tool for the structure determination of catalyst samples. There are several reviews [2,5–7] and international workshops [8–10] about the XAFS investigation for the catalyst field. In this short review, I will describe the most recent topics concerning the present status of XAFS work in the catalyst field in Japan. The work that I have reviewed here was carried out in the Photon Factory, the 20th anniversary of which was celebrated this year (2002). It has matured suitably for the investigations in material sciences.

2. *In situ* XAFS under flow and high-pressure conditions

X-rays can easily penetrate into materials and one can measure XAFS signals in the presence of gas phase. Therefore, XAFS is capable of carrying out the *in situ* characterization of catalysts. The catalyst structure varies in the process of the reaction. For example, the CO insertion reaction on a Rh dimer catalyst on SiO_2 occurs with the dynamic breakage and creation of Rh–Rh bonds [9–10]. Since XAFS requires a strong X-ray source like a synchrotron radiation, where the experimental facility (called an experimental hall) is shared by scientists in many fields, XAFS measurement stations with gas handling systems are required in order to carry out the *in situ* experiment under flow and high-pressure reaction conditions for safety reasons. However, it is not so convenient to fix the gas handling system at a particular experimental station because the experimental station cannot be shared by other experiments than the *in situ* XAFS work and because the station should cover a wide photon energy range between 2 (S K-edge) and 30 (Sn K-edge) keV or more. Bando, Shirai, Ichikuni, and Kubota have collaborated to construct a mobile and a knockdown type of the *in situ* XAFS measurement system [14,15]. Figure 1 shows the flow-line system used for the XAFS measurement under high-pressure reaction conditions. Since every part of the flow system is easily dissembled and compactly packed, it is mobile from one beam line to another. Consequently, one can select a beam line suitable for the sample, and the flow system is assembled just before the beam time so as not to interfere in other types of experiments. The leakage is rigorously tested by pressurized He and a He detector before using high-pressure hazardous and flammable gases such as H_2, H_2S, thiophene, CO, and CO_2. In case of sudden leakage, gas sensors and detectors are placed at many parts of the joints and the ppm order leakage is always monitored. The gases coming out of the measurement cell are analyzed in real time by gas chromatography or mass spectroscopy. The exhaust gas is totally burned with a converter and is vented to a duct. When a hydrodesulfurization reaction is carried out, the unreacted sulfur compounds are first converted to H_2S and then adsorbed on the ZnO.

* To whom correspondence should be addressed.
E-mail: askr@cat.hokudai.ac.jp

1384-6574/03/0900-0177/0

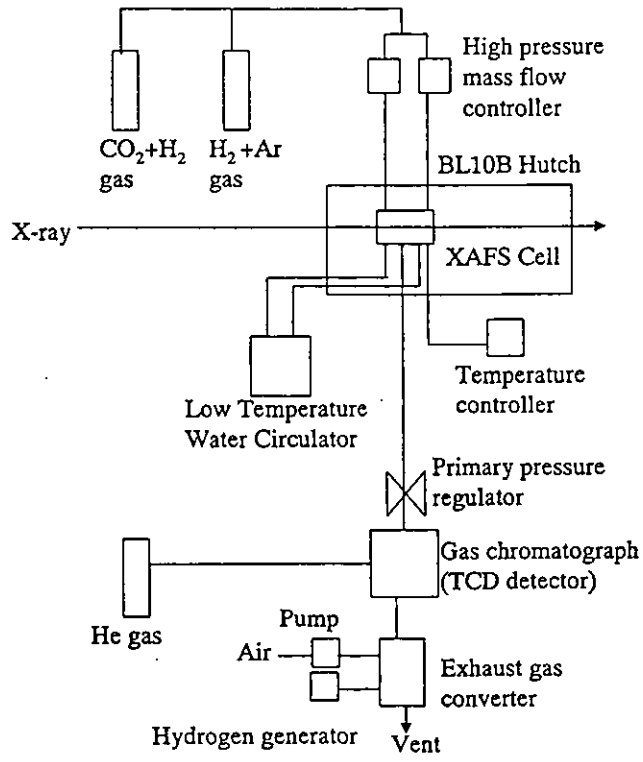

Figure 1. A mobile and knockdown gas flow system for *in situ* XAFS measurement (From reference [14]).

Figure 2 shows a high-pressure XAFS cell. In the *in situ* measurement, the selection of the X-ray windows is the next problem in carrying out the high-pressure reaction. Beryllium windows were adopted in a previous work [16]. But the Be is toxic and becomes fragile under the H_2 atmosphere to form BeH_x. Bando *et al.* used acrylic plastic plates with a thickness of 3 mm and a diameter of 20 mm [14]. The windows are tolerable up to 6 MPa and are transparent for X-rays above 8 keV. To prevent contact of the windows with the hot gases, the gases were supplied from both sides near the windows to the center (a hot place). The windows are also cooled by flowing water. However, one has to be careful about the radiation damage of the acrylic windows when they are exposed to a high-intensity X-ray beam ($>10^{14}$ cm^{2}s^{-1}) for a long time (>20 h) [17]. Bando *et al.* investigated the structural change of Rh particles in NaY during the CO_2 hydrogenation reaction [14]. Figure 3 shows Fourier transforms of the Rh catalysts in NaY zeolite during reduction processes. Before reduction, the Rh–O and Rh–Rh were found at 0.16 and 0.27 nm (phase shift uncorrected), indicating the presence of Rh_2O_3. The sample was heated up to 404 K; the Rh–O peak was remarkably reduced. At 472 K, the Rh–Rh peak appeared at 0.23 nm, well corresponding to the bond length of Rh metal particles. Further increase in the reduction temperature suppresses the Rh–Rh peak height owing to the Debye Waller factor. *In situ* XAFS provides the real structure of the catalyst under real catalytic conditions.

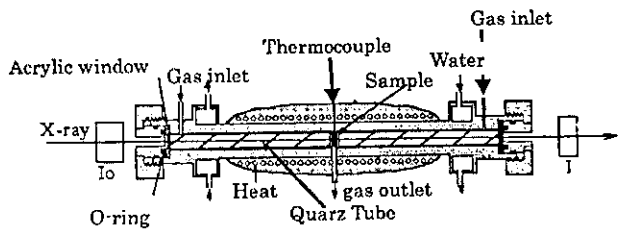

Figure 2. An *in situ* XAFS measurement cell designed for high-pressure flow reaction conditions (From reference [14]).

3. Time-resolved XAFS investigations

Since a monochromator is moved point-by-point to select X-ray energy in a conventional XAFS measurement [18], it takes at least a few minutes to acquire a whole XAFS spectrum. A more rapid data acquisition method is required to follow the dynamic structure change of active sites and to investigate the short-lifetime transient species. There are four methods for XAFS measurements with a high time resolution. One is a pump-probe method that can be applied to a conventional XAFS system and a fluorescence XAFS [19–21]. However, this method is only applicable to repeatable reactions. The second one is a quick XAFS in which a monochromator is continuously rotated by a DC motor or a piezo driver [22]. One can achieve a millisecond order time resolution [23]. In the QXAFS, the fluorescence detection is possible and the XAFS signal was recorded for a very diluted system (<10 mmol l^{-1}) [24]. The third way is a dispersive method, which I will describe in detail here. The last one is a combination of the quick XAFS and the dispersive XAFS proposed by Oyanagi *et al.* [25], in

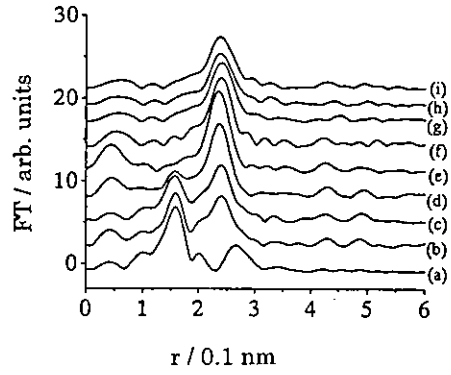

Figure 3. Fourier transforms of the *in situ* XAFS spectra for the Rh/NaY in the reduction processes. (a) r.t. in N_2, (b) 297 K, (c) 338 K, (d) 404 K, (e) 472 K, (f) 540 K, (g) 612 K, (h) 679 K and (i) 707 K in the flow 20% H_2 balanced with Ar. The flow rate was 100 ml/min (From reference [14]).

which the X-ray energy is dispersed by a polychromator and is scanned by a rapidly moving slit in front of the sample.

The dispersive XAFS is one of the most promising techniques for investigating the fast data acquisition for a very rapid change of active sites. It was originally proposed by Matsushita *et al.* in the early '80s in order to obtain a laboratory-scale XAFS in a short time [26]. Nomura, Yamaguchi, Inada, Suzuki, Shido, and Iwasawa have improved the system suitable for the *in situ* XAFS measurements of the catalysis system [27]. Figure 4 shows the dispersive XAFS setup [28]. White and almost parallel X-rays with various energies hit a Si bent crystal, called a polychromator. The X-ray energies are dispersed by the polychromator according to the path because the Bragg angles of the X-rays against the curved polychromator surface are gradually varied from one edge to the other. The X-rays are focused at one point on the sample and then dispersed onto a position-sensitive detector. Because the X-ray wavelengths are different from position to position on the detector, one can get a whole spectrum at once.

Whole spectra of Cu in ZSM-5 and $Mo(CO)_6$ in Y zeolite have been measured in a second or less [29,30]. Figure 5 shows time-resolved spectra of the Cu in ZSM-5 during a hydrogen reduction process with a 1-s interval. The Cu in ZSM-5 was prepared by an ion-exchange method using a copper nitrate solution (Cu/Al × 200 = 84%) [29]. The sample was reduced with a heating rate of 5 K/min in the presence of 5.3 kPa H_2. Cu^{2+} was finally reduced to Cu^0. However, the intermediate state, Cu^+, was found in the temperature range of 400–550 K. The bond distances for Cu^{2+}–O and Cu^+–O were both 0.195 nm and the coordination number of Cu–O decreased with the reduction of Cu species. The Cu–Cu bonds with metallic distances were found at 550 K at 0.255 nm. The Cu–Cu coordination number increased with the reduction temperature.

4. Polarization-dependent total reflection fluorescence XAFS

Synchrotron radiation is linearly polarized and XAFS has the following polarization dependence:

$$\chi(k) = \sum_i 3 \cos^2 \theta_i \cdot \chi_i(k) \qquad (1)$$

where $\chi(k)$, $\chi_i(k)$, and θ_i are the total XAFS oscillation, an XAFS oscillation accompanied by the ith bond, and the angle between the ith bond and the polarization vector of the X-ray. Thus, the XAFS oscillation is enhanced three times when the bond direction is parallel to the polarization vector, while it is not enhanced for the bond direction perpendicular to the polarization vector. When XAFS is applied to a powder sample, polarization dependence is averaged over all directions. On the other hand, when it is applied to a single crystal, one can have a local structure dependent on the polarization direction. When a single crystal oxide on which metal or metal oxide species are deposited is used as a model-supported catalyst, three-dimensional local structures of the dispersed species can be obtained by the polarization-dependent XAFS measurement. However, the problem is the low concentration of the surface species on the single crystal surface, which is usually on the order of 10^{13-15} cm^{-2}. In order to measure dilute systems, one uses a fluorescence method [23]. The lowest limit of the fluorescence method is determined by the scattering X-ray coming from the substrate bulk. One should adopt a total reflection mode. At glancing incident conditions of X-rays, they undergo total reflection and can penetrate only by 2.0–3.0 nm, which tremendously reduces the scattering X-rays from the bulk. As a result, the detection limit is decreased to 10^{13-14} atoms. We have developed an *in situ* polarization-dependent total reflection fluorescence (PTRF-XAFS) XAFS system, as shown in figure 6, to investigate a model system for supported metal catalysts [32,33]. The sample is set at the UHV-compatible high-precision 6-axis goniometer, in which three different orientations of the sample against the electric vector are realized. The sample can be heated up to 600 K. The whole chamber can be evacuated to 10^{-8} Pa and reaction gases can be introduced up to 1 atm. Figure 7 shows the XAFS oscillations for Cu on TiO_2(110) reduced at 363 K prepared from $Cu(DPM)_2$. The polarization dependence of XAFS oscillations indicated the presence of anisotropic structures. Curve-fitting analyses of XAFS oscillations for Cu/TiO_2 reduced at 363 K indicated that the Cu trimer was formed on the TiO_2 surface as shown in figure 8 [34]. The structures of Mo oxides on MgO, Al_2O_3, and TiO_2 single crystals also have been determined by this method [35,36]. The structures varied with the chemical circumstances of the

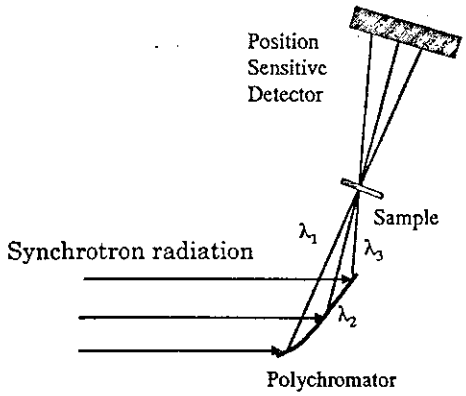

Figure 4. A setup for the dispersive XAFS (From reference [28]).

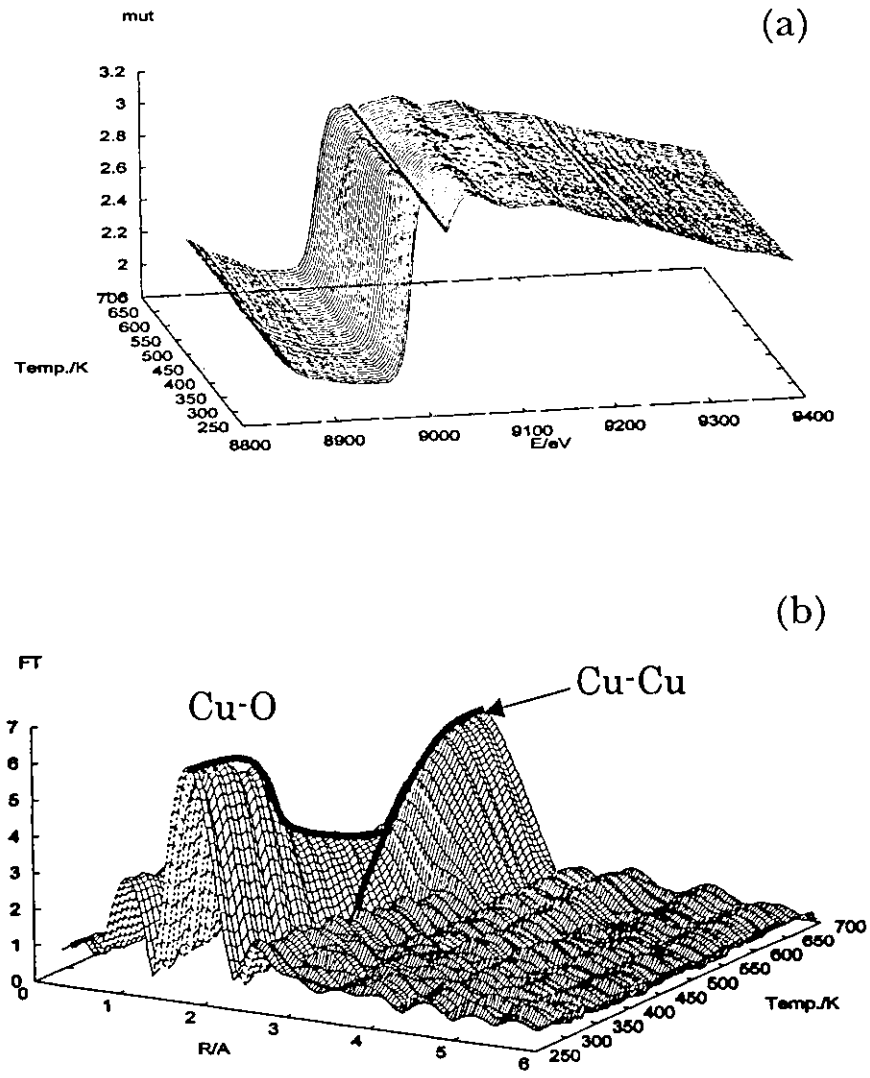

Figure 5. (a) Dispersive XAFS spectra of Cu/ZSM-5 in the temperature-programmed reduction process. Time interval for each spectrum is 1 s. The heating rate is 5 K/min. (b) Corresponding Fourier transforms of dispersive XAFS spectra. A peak at 1.8 Å corresponds to Cu–O bonds and a peak at 2.2 Å to Cu–Cu bonds (From reference [29]).

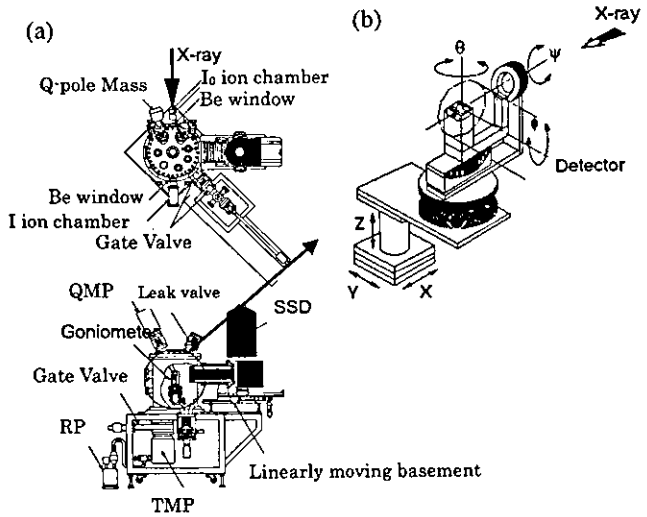

Figure 6. (a) A sketch of an *in situ* polarization-dependent total-reflection fluorescence XAFS chamber and (b) a UHV-compatible high-precision 6-axis goniometer (From reference [32]).

support surfaces. On a basic support like MgO, an isotropic MoO_4^{2-} structure was stabilized, while the more acidic Al_2O_3 and TiO_2, octahedral-like structures were preferred. The octahedral dimer with its Mo–Mo bond along the $[1\bar{1}0]$ direction was found especially on the TiO_2 [36].

5. Future aspects

XAFS is now one of the most powerful tools for the catalysts' characterization, especially under *in situ* conditions. Time-resolved XAFS measurement is a promising technique. Time resolution is second–millisecond at moment. But a new brilliant X-ray source will improve the time resolution, and by adopting the pump-probe method, nanosecond time resolution will be possible. Such a high time resolution is important for detecting reaction intermediates. On the other hand, the

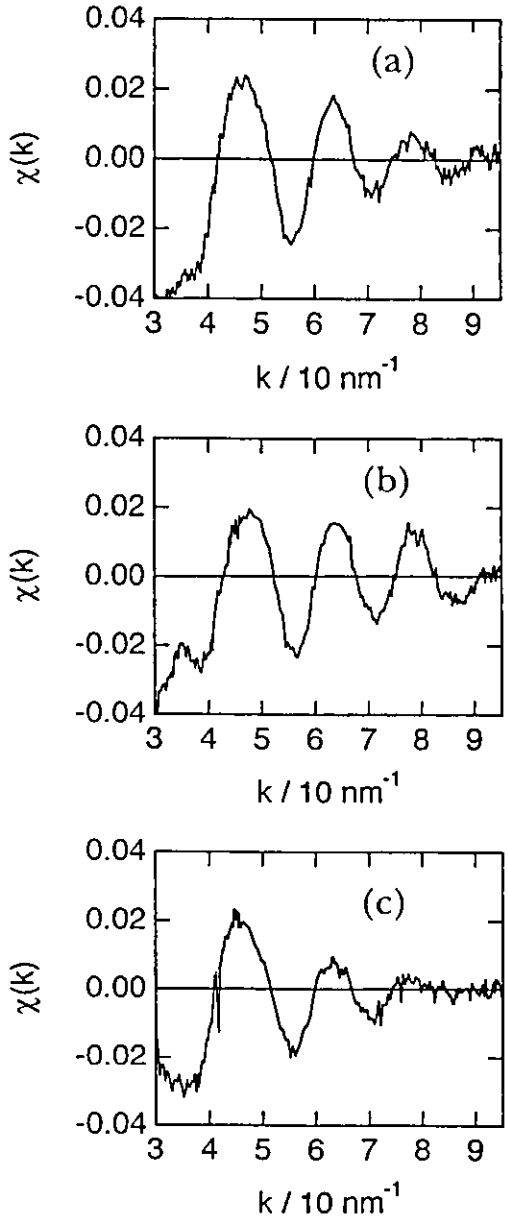

Figure 7. Polarization-dependent XAFS oscillations of Cu on TiO_2(110) after reduction at 363 K. (a) E //[110], (b) E //[001], (c) E // [110] (From reference [34]).

spatial resolution of conventional XAFS is 1–10 mm. By focusing the X-ray beam, spatial resolution with a micrometer is now possible. These spatial-resolved methods will be applied to micro- or nanoparticles or microdomains. By the combination of a tilt stage and polarization dependence of XAFS, one will have three-dimensional structural analysis of a single nanoparticle. The third resolution—an energy resolution—draws big attention. De Groot *et al.* gives a good review about the high-energy resolution and XAFS to show a possibility of site- and element-selective XAFS [37]. Moreover, they show the possibility of measuring the low Z element or

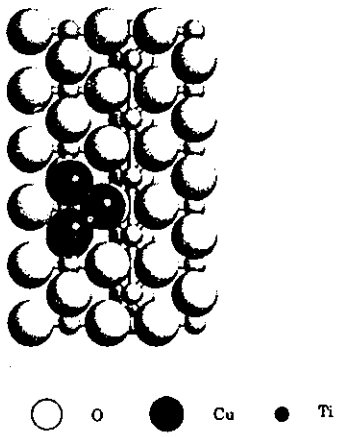

Figure 8. A proposed model structure for Cu species on a TiO_2(110) surface (From reference [34]).

shallow core edges (L, M edge) using a hard X-ray. The exploitation of these three kinds of energy resolution will be the next challenge to XAFS spectroscopy.

Acknowledgments

This work was financially supported by CREST of JST, Japan, and Grant-in-aid (B)(2) 11440202, from JSPS and the International Joint Research Grant of NEDO, Japan.

References

[1] D.C. Koningsberger and R. Prins, *X-ray Absorption, Principles, Applications, Techniques of EXAFS, SEXAFS, and XANES*, (John Wiley & Sons, 1988).
[2] Y. Iwasawa (ed.), *X-ray Absorption Fine Structure for Catalysts and Surfaces*, (World Scientific, Singapore, 1996).
[3] D.E. Sayers, E.A. Stern and F.W. Lytle, Phys. Rev. Lett. 27 (1971) 1204.
[4] T. Ohta and M. Nomura (eds), *Proceedings of 11th International Conference on XAFS* (Ako, 2000); which appeared in J. Synchrotron Radiat. 8 (2001) 47–1014.
[5] J.C. Bart, Adv. Catal. 34 (1986) 203.
[6] J.C. Bart and G. Vlaic, Adv. Catal. 35 (1987) 1.
[7] D.C. Koningsberger (ed.), Top. Catal. 10 (2000).
[8] Y. Iwasawa (ed.), The Proceedings are available in Catal. Lett. 20 (1993).
[9] Hightower and Joyner (eds), The Proceedings are available in Catal. Today 39 (1998).
[10] J.M. Thomas and K. Asakura (eds), The Proceedings are available in Top. Catal. 18 (2002).
[11] K. Asakura, K.K. Bando, K. Isobe, H. Arakawa and Y. Iwasawa, J. Am. Chem. Soc. 112 (1990) 3242.
[12] K. Asakura, K.K. Bando, Y. Iwasawa, H. Arakawa and K. Isobe, J. Am. Chem. Soc. 112 (1990) 9096.
[13] K.K. Bando, K. Asakura, H. Arakawa, K. Isobe and Y. Iwasawa, J. Phys. Chem. 100 (1996) 13636.
[14] K.K. Bando, T. Saito, K. Kato, T. Tanaka, F. Dumeignil, M. Imamura, N. Matsubayashi and H. Shimada, J. Synchrotron Radiat. 8 (2001) 581.
[15] Information about the in-situ XAFS group is available in homepage http://www.aist.go.jp/kk.bando/index.html.

[16] D. Bazin, H. Dexpert and J. Lynch, in *X-ray Absorption Fine Structure for Catalysts and Surfaces*, (ed.) Y. Iwasawa (World Scientific, Singapore) p. 113.
[17] K.K. Bando, T. Kubota and T. Kawai, private communications.
[18] M. Nomura, in *X-ray Absorption Fine Structure for Catalysts and Surfaces*, (ed.) Y. Iwasawa (World Scientific, Singapore, 1996) p. 92.
[19] H. Oyanagi, A. Kolobov and K. Tanaka, J. Synchrotron Radiat. 5 (1998) 1001–1003.
[20] L.X. Chen, J. Electron Spectrosc. 119 (2001) 161–174.
[21] G. Jennings, W.J.H. Jager and L.X. Chen, Rev. Sci. Instrum. 73 (2002) 362–368.
[22] R. Frahm, Rev. Sci. Instrum. 60 (1989) 2515.
[23] J.D. Grunwaldt, D. Lutzenkirchem-Hecht, M. Richwin, S. Grundmann, B.S. Clausen and R. Frahm, J. Phys. Chem. 105 (2001) 5161.
[24] D. Lutzenkirchen-Hecht, S. Grundmann and R. Frahm, J. Synchrotron Radiat. 8 (2001) 6.
[25] H. Oyanagi, in *X-ray Absorption Fine Structure for Catalysts and Surfaces*, (ed.) Y. Iwasawa (World Scientific, Singapore, 1996) p. 2, 383.
[26] U. Kaminaga, T. Matsusita and K. Kohra, Jpn. J. Appl. Phys. 20 (1981) L355.
[27] T. Shido, A. Yamaguchi, Y. Inada, K. Asakura, M. Nomura and Y. Iwasawa, Top. Catal. 18 (2002) 53.
[28] A. Yamaguchi, Doctor Thesis (The University of Tokyo, Tokyo, 2001).
[29] A. Yamaguchi, T. Shido, Y. Inada, T. Kogure, K. Asakura, M. Nomura and Y. Iwasawa, Bull. Chem. Soc. Jpn. 74 (2001) 801–808.
[30] A. Yamaguchi, T. Shido, Y. Inada, T. Kogure, K. Asakura, M. Nomura and Y. Iwasawa, Catal. Lett. 68 (2000) 139; A. Yamaguchi, A. Suzuki, T. Shido, Y. Inada, K. Asakura, M. Nomura and Y. Iwasawa, Catal. Lett. 71 (2001) 203–208.
[31] S.M. Heald, in *X-ray Absorption Fine Structure*, (eds) D. C. Koningsberger and R. Prins (John Wiley & Sons, New York, 1988).
[32] W.-J. Chun, Y. Tanizawa, T. Shido, Y. Iwasawa, M. Nomura and K. Asakura, J. Synchrotron Radiat. 8 (2001) 168.
[33] W.-J. Chun, Doctor Thesis (The University of Tokyo, Tokyo, 1997).
[34] Y. Tanizawa, W.-J. Chun, T. Shido, K. Asakura and Y. Iwasawa, J. Synchrotron Radiat. 8 (2001) 508.
[35] K. Asakura and K. Ijima, J. Electron Spectrosc. 119 (2001) 185.
[36] W.-J. Chun, K. Asakura and Y. Iwasawa, J. Phys. Chem. 102 (1998) 9006.
[37] F.M.F. de Groot, Top. Catal. 10 (2000) 179.

X-ray Absorption Fine Structure Studies on the Local Structures of Ni Impurities in a Carbon Nanotube

Kiyotaka Asakura,[†] Wang-Jae Chun,[†,††] Kazuyuki Tohji,[†††] Yoshinori Sato,[†††] and Fumio Watari[††††]
[†]*Catalysis Research Center, Hokkaido University, Sapporo, Hokkaido 001-0021*
[††]*Core Research for Evolutional Science and Technology, Japan Science and Technology Corporation, Sapporo, Hokkaido 001-0021*
[†††]*Graduate School of Environmental Studies, Tohoku University, Aoba, Sendai, 980-8579*
[††††]*Graduate School of Dental Medicine, Department of Biomedical, Dental Materials & Engineering, Hokkaido University, Kita 13 Nishi 7 Sapporo, Hokkaido 060-8586*

(Received October 21, 2004; CL-041243)

Local structure around Ni impurities in a carbon nanotube was studied by X-ray absorption fine structure (XAFS). The Ni was present in the form of Ni particles before the purification process. After the purification Ni content was decreased to a few hundreds ppm. The Ni K-edge XAFS could be measured by a 19 element solid-state detector. The Ni species was strongly bound to the carbon of the carbon nanotube with a Ni–C covalent bonds at 0.173 nm.

Carbon nanotubes draw much attention as new materials, which have wide applications to many fields such as electric devices, hydrogen storage materials, field emission display, AFM tip, and so on.[1] Since carbon nanotubes are composed of only carbon atoms and are expected to have biocompatibility, the researches for the biological application have been started such as a drag delivery system, scaffolds for cell engineering, artificial bones, dental roots, and cell culture media.[2] Chemical vapor deposition (CVD) synthesis method using catalysts such as Ni, Fe, Fe–Ni, and Ni–Mo is one of promising methods for large-scale production of carbon nanotubes.[3] Ni is one of the best catalysts to produce carbon nanotubes but it often shows toxic properties to a living body. Although most of Ni in the carbon nanotube can be removed by the HCl treatment, it is important to know the metabolism, chemical state, and structure of Ni impurity left in the carbon nanotubes after the HCl treatment in order to apply the nanotubes to medical and biological fields safely. In this paper, we report the characterization of the chemical state of residual Ni species before and after the purification processes of a carbon nanotube by XAFS (X-ray absorption fine structure) technique. Because the amount of Ni species after the purification is about a few hundred ppm, it is difficult to estimate the Ni chemical state by conventional techniques. We carried out fluorescence XAFS analysis of Ni impurity in the carbon nanotube. We found that the Ni species was strongly fixed to the carbon of a carbon nanotube through a Ni–C covalent bond.

Carbon nanotube was synthesized by a CVD method using Ni catalyst. It was purified by a calcination followed by 6 M HCl treatment for 6 h in order to remove the carbon nanoparticles and Ni catalysts.

XAFS measurements were carried out at BL9A of the Photon Factory in Institute for Structure Material Science (KEK-PF) using a Si(111) double crystal monochromator.[4] (99G280, 2001G287) The incident and transmitted X-rays were monitored by ionization chambers filled with nitrogen. The fluorescence X-ray was detected by a 19 element SSD (solid state detector) (Camberra Co.) The dead times of SSD were corrected according to the literature.[5] The XAFS analyses were carried out by REX2000 (Rigaku Co) using phase shift and amplitude functions derived from FEFF8.[6,7]

Figure 1 showed the Fourier transforms of Ni K-edge XAFS oscillations before the purification over $k = 30$–$150\,\mathrm{nm}^{-1}$. We measured the XAFS oscillation in a transmission mode because we had an enough edge jump. We found several peaks. The first and main peak appeared at 0.25 nm, which corresponded to that of the Ni–Ni distance in the first shell of Ni metal. The longer Ni–Ni peaks clearly appeared, which were corresponding to the 2nd, 3rd and 4th shells in the Ni fcc structure. The curve fitting analysis showed that the coordination number and bond distance of the first shell Ni–Ni bond were 12 and 0.248 nm, respectively, indicating that the Ni was present in a metal particle larger than 5 nm judging from the coordination numbers of the first and the higher shells which were almost equal to that of the bulk Ni species.[8]

When the Ni metal particles were removed by the HCl treatment, we could not observe Ni K-edge in a transmission mode any more. Thus we used a fluorescence mode to obtain Ni XAFS oscillations. According to the Ni Kα fluorescence peak intensity, the amount of Ni can be estimated to be about a few hundred ppm. Figure 2 shows the X-ray near edge structure of Ni species in the carbon nanotube before and after the HCl treatment to-

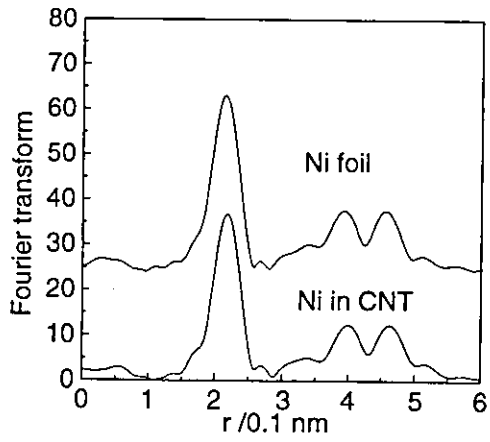

Figure 1. Fourier transforms of XAFS oscillations for Ni catalysts in the carbon nanotube and Ni foils.

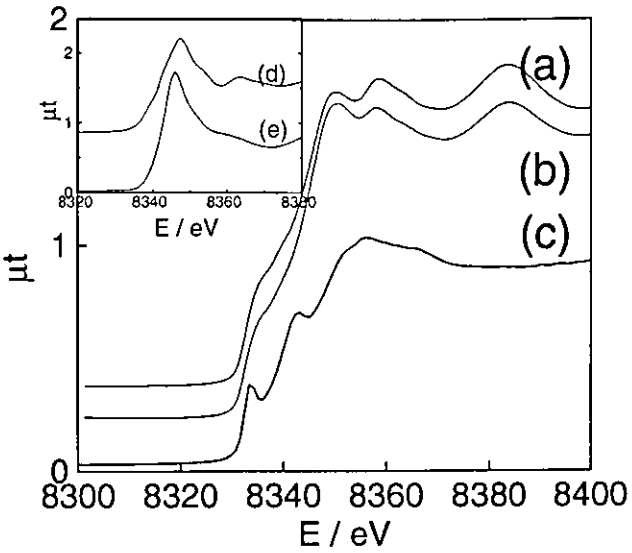

Figure 2. Ni K-edge XANES of (a) Ni foil, (b) Ni species in the carbon nanotube before purification, and (c) that after the purification. (d) and (e) in the inset showed XANES spectra for NiO and $Ni(NO_3)_2 \cdot 9H_2O$.

gether with reference compounds. The XANES (X-ray absorption near edge structure) spectrum after the HCl treatment was completely different from that before the HCl treatment and Ni foil, indicating that the metallic Ni particles were completely removed by the HCl treatment. The XANES spectrum of the sample after the HCl treatment was different from those of NiO and $Ni(NO_3)_3 \cdot 9H_2O$. The residual Ni species was not simple oxide or aquo complex ions. Peaks in the XANES spectrum appeared at the similar positions as in the spectrum of the deactivated Ni catalyst after the CH_4 decomposition reaction though the peak heights were much stronger in the present spectrum.[9]

Figure 3 shows the Fourier transforms of Ni K-edge XAFS of Ni species in the carbon nanotube after the HCl treatment. Peaks appear at 0.16 and 0.22 nm. We carried out curve fitting analysis for the first shell assuming Ni–C bond. The bond distance and coordination number were 0.177 nm and 1.5, respectively. The second shell peak could be assigned to Ni–Ni at 0.247 nm with its coordination number 0.8. Ni–C distance 0.177 nm was smaller than 0.186 and 0.184 nm found in Ni_3C and $Ni(CO)_4$, respectively. Thus the Ni species was fixed strongly to carbon nanotube through a covalent bond. Since carbon nanotubes were stable in the living body, Ni impurity may stay there for a long time and may bioaccumulate. We recommend that the Ni catalyst should not be used to the production of the carbon tube if it is used as a biomaterial.

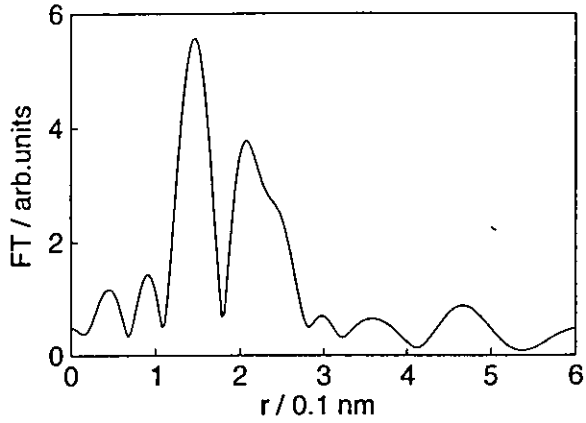

Figure 3. Fourier transform of Ni K-edge EXAFS for the Ni species in the carbon nanotube after the HCl treatment.

References

1 P. J. F. Harris, "Carbon Nanotubes and Related Structures: New Materials for the Twenty-first Century," Cambridge University Press, Cambridge (1999).
2 "Nanotoxicology and Development of Carbon Nanotubes and Nano/Micro Particles for Biomedical Applications," ed. by F. Watari, Springer Verlag, Berling, to be published.
3 M. Endo, Y. A. Kim, T. Hayashi, T. Yanagisawa, H. Muramatsu, M. Ezaka, H. Terrones, M. Terrones, and M. S. Dresselhaus, *Carbon*, **41**, 1941 (2003).
4 M. Nomura, *KEK Report*, **98-194**, 1 (1998).
5 M. Nomura,*KEK Report*, **98-4**, 1 (1998).
6 K. Asakura, "X-ray Absorption Fine Structure for Catalysts and Surfaces," ed. by Y. Iwasawa, World Scientific, Singapore (1996), pp 33–58.
7 S. I. Zabinsky, J. J. Rehr, A. Ankudinov, R. C. Albers, and M. J. Eller, *Phys. Rev. B*, **52**, 2995 (1995).
8 R. B. Greegor and F. W. Lytle, *J. Catal.*, **63**, 476 (1980).
9 S. Takenaka, H. Ogihara, and K. Otsuka, *J. Catal.*, **208**, 54 (2002).

Published on the web (Advance View) February 12, 2005; DOI 10.1246/cl.2005.382

Production of monodispersed particles by using effective size selection

O. Perales-Perez,[a] H. Sasaki, and A. Kasuya
Center for Interdisciplinary Research Tohoku University, Aramaki aza Aoba, Sendai 980-8578, Japan

B. Jeyadevan and K. Tohji
Department of Geosciences and Technology Tohoku University, Sendai 980-8579, Japan

T. Hihara and K. Sumiyama
Nagoya Institute of Technology, Nagoya 466-8555, Japan

In this article we report the results of two size selection methods that are based on interfacial interaction between nanosize particles, magnetite in this case, anionic surfactants, and nonpolar solvents. It is proposed that by selecting a suitable surfactant type and/or conditions to modify the particle–particle separation distance, only smaller particles can be stabilized against aggregation and settling making a size sensitive separation possible. Using this phenomenon, an effective size selection at the nanosize level has been achieved and the preliminary results are presented here. Depending on the conditions, stable suspensions of nearly monodispersed nanoparticles of magnetite (diameter less than 10 nm and standard deviation, σ, below 0.2) were obtained from polydispersed powders (less than 40 nm in diameter and σ around 0.6) synthesized from aqueous solutions at 25 °C. Magnetization measurements of the fractions confirmed the effectiveness of the developed size selection methods. © *2002 American Institute of Physics.*
[DOI: 10.1063/1.1452193]

I. INTRODUCTION

Intensive investigations have been carried out to control the particle size and the size distribution during the synthesis of various nanosize materials.[1,2] A serious disadvantage of this option is the low yield of product due to the low concentration of reactants affordable in the majority of cases. An alternative approach for the production of monodispersed particles is the application of a size-selection method for polydispersed powders. In this way, larger amounts of materials could be treated and almost monodispersed particles of desired sizes would also be expected. The present article reports the results of two size selection methods that are based on the control of interfacial interaction between nanosize particles, using either suitable ionic surfactants or nonpolar solvents. Using these methods, stable suspensions of monodispersed magnetite nanoparticles (standard deviation, σ, below 0.2) having various diameters, were obtained.

II. EXPERIMENT

A. Materials

The magnetite used for the size-selection tests was produced at 25 °C by adding NaOH solution into a Fe(II)–Fe(III) bearing solution, mole ratio Fe(III)/Fe(II)=2, until *p*H 12 was reached.

In the size-selection tests the following anionic surfactants were evaluated: Na-oleate, $C_{17}H_{33}COONa$, and the Na-salts of stearic (SASS, $C_{17}H_{35}COONa$), palmitic (PASS, $C_{15}H_{31}COONa$), myristic (MASS, $C_{13}H_{27}COONa$), and lauric (LASS, $C_{11}H_{23}COONa$) acids. Toluene was used as the dispersing media in all cases. Acetone was used to get the size sensitive phase separation from starting polydispersed suspensions.

B. Size selection procedures

In this article two size-selection methods will be introduced.

(i) Method A: fixed amounts of magnetite were contacted with aqueous solutions of the anionic surfactants at 90 °C for 1 h. Except for Na-oleate solutions (when the *p*H was 9.5), all other surfactant solutions exhibited a *p*H between 10.6 and 10.8 at 25 °C. The evaluated surfactant/magnetite w/w ratios were 20 and 30% for each type of surfactant. In a different set of tests, the surfactant/magnetite ratios were evaluated on a molar basis. After successive washing cycles, the surfactant- coated samples were dried at 60 °C, and dispersed in toluene. The suspensions prepared under this condition were left overnight to facilitate phase separation.

(ii) Method B: A stable suspension of Na oleate-coated magnetite was contacted with controlled volumes of acetone and sonicated to homogenize the mixture. After a suitable "settling time" a size-sensitive phase separation became evident. The supernatant, containing suspended particles, was separated from the sediment by decantation. The corresponding settled particles accounted for the classified size fractions numbered from 1 to 4 in Table I. The supernatant was treated again with acetone and the reported above phase separation cycle was repeated for four times. The suspension coming from the fourth cycle was the final product of this size selection method.

Stable suspensions and settled particles obtained by methods "A" and "B" were analyzed using high-resolution

[a]Electronic mail: ojpp@peru.com

TABLE I. Size selection by acetone treatment.

Product	Acetone/toluene, v/v	Diameter (nm)	σ
1	0.2	12.7	0.27
2	0.4	9.2	0.27
3	0.6	9.0	0.20
4	0.9	6.9	0.20
5	···	5.9	0.16

transmission electron microscopy (HRTEM) and energy dispersive spectroscopy for their particle size and chemical composition. The magnetization measurements were carried out by the superconducting quantum interference device technique.

III. RESULTS AND DISCUSSION

A. Size selection at the nanosize level

1. Method A

The histograms shown in Fig. 1 summarize the main results obtained when a single-step separation was attempted. When the *p*H of the Na-oleate aqueous solution was 10.8 for a surfactant/magnetite weight ratio of 30% (obtained by estimating of the particle size to be 10 nm) almost all particles were stabilized in suspension. Consequently, any size separation was not possible. However, a reasonably good size separation was obtained when the surfactant/magnetite ratio was decreased down to 20% or the *p*H of the surfactant aqueous solution was 9.5. These conditions may have favored a size-sensitive phase separation by affecting the extent of surfactant adsorption, i.e., the degree of surface coverage. Although a size selection was achieved in both cases, the stable suspensions still exhibited a wide size distribution. On the contrary, stable and almost monodispersed suspensions of magnetite were obtained when the sodium salts of stearic or myristic acids, which exhibit only single C–C bonds in their hydrophobic tails, were employed. The HRTEM micrograph given in Fig. 1 reveals that a self-assembled arrangement of magnetite particles of 5.1 nm in diameter, D, was obtained when stearic acid Na-salt was

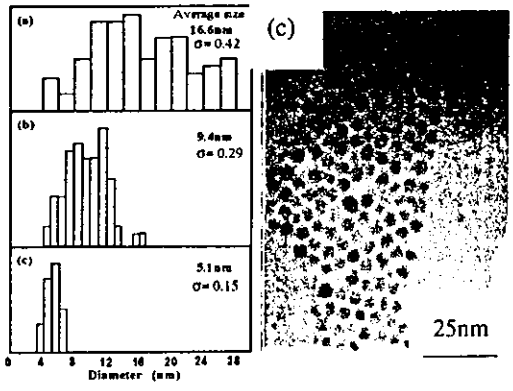

FIG. 1. Histograms of particles treated with (a) Na-oleate (settled), (b) Na-oleate (suspended), and (c) SASS (suspended). The HRTEM corresponds to sample (c).

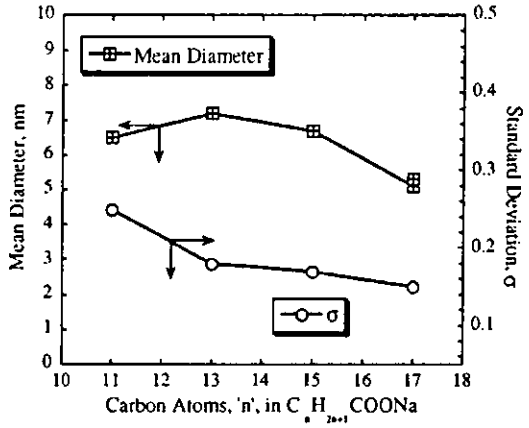

FIG. 2. Particle size and standard deviation, σ, of particles suspended in surfactants with different number of carbon atoms, C_n.

used. The suspension was stable even after prolonged periods of time (longer than 6 months). The settled fraction included particles with large diameters and exhibited a distribution similar to the histogram (a) in Fig. 1.

A different set of experiments was designed to confirm the preliminary trends and get more detailed information about the effect of surfactant chain length (C_n, where "n" is the number of carbon atoms) on the particle size of suspensions. In these experiments the S/F ratio was 0.23 on a molar basis and the *p*H of the magnetite-surfactant suspension 10.8. Other conditions were the same as detailed for method A.

The results, shown in Fig. 2, suggest that the surfactants with longer chain length would favor the stabilization of smaller particles. Moreover, the decrease in the size of the particles stabilized in suspension went in parallel with the rise in their monodispersity as evidenced by the lowering in the standard deviation for the size distribution, σ. A preliminary interpretation attributes the viability in size selection to the affinity of active surfaces of smaller particles to certain types of surfactant structures, a phenomena that could also be related to the presence of micelles in solution as expected from the low critical micell concentration values for surfactants with longer chain lengths.

2. Method B

Acetone was added in 1 ml increments to a stable suspension of magnetite in toluene (10 ml, magnetite/toluene = 0.1 on a weight basis) resulted in a size-sensitive phase separation from a starting polydispersed suspension (σ=0.4), as shown in Table I and Fig. 3.

It is proposed that the addition of acetone would have caused the interparticle separation distance to change by contraction of the hydrophobic tail, conducive to a size selective coagulation. Accordingly, only smaller particles could have been stabilized against coagulation whereas bigger ones should have approached one to each other at a distance short enough to favor the predominance of the size-dependent magnetic dipolar and/or van der Waals attractive interactions that caused coagulation and subsequent settling. The estimations of the energetic interactions involving size/distance de-